Remobilization and eruption of an upper crustal cumulate mush at the Singkut caldera (North Sumatra, Indonesia)

Francesca Forni [a,b,*], Marcus Phua [b], Olivier Bernard [c], Maria Giuditta Fellin [d], Jeffrey Oalmann [e], Colin Maden [d], Hamdi Rifai [f], Caroline Bouvet de Maisonneuve [b]

[a] Dipartimento di Scienze della Terra "Ardito Desio", Università degli Studi di Milano, 20133 Milan, Italy
[b] Earth Observatory of Singapore and Asian School of the Environment, Nanyang Technological University, Singapore 639798, Singapore
[c] Institut de Physique du Globe de Paris, Université de Paris Cité, 75238 Paris Cedex 0, France
[d] Institute of Geochemistry and Petrology, ETH Zurich, 8092 Zürich, Switzerland
[e] Centre for Ore Deposits and Earth Sciences, University of Tasmania, Private Bag 79, Hobart, Tasmania 7001, Australia
[f] Department of Physics, Universitas Negeri Padang, Padang 25131, Indonesia

A R T I C L E   I N F O

A B S T R A C T

Understanding the conditions and timescales of storage and remobilization of magma bodies in the upper crust is key to interpreting the signals of potential reawakening at active volcanoes. In this paper, we provide the first volcanological and petrochronological characterization of the Singkut caldera, a young volcanic system located in northern Sumatra (Indonesia), in close proximity to Medan, one of the country's most populous cities. Singkut formed at ~44 ka during a VEI 6 explosive eruption that deposited at least ~26 km³ of tephra (dense rock equivalent, DRE). The cataclysmic eruption was preceded by >200 ky of mostly effusive pre-caldera activity and followed by effusive to mildly explosive post-caldera activity. The lavas and pumices have high crystallinity (up to 62% crystals) with andesitic to dacitic bulk-rock composition and rhyolitic glass. Mineral textures and matrix glass compositions indicate resorption of quartz, plagioclase and zircon. Zircon crystallization ages show a complete overlap with the eruption ages in pre-caldera lavas, while a time gap in zircon crystallization (>50 ky) is identified in the caldera-forming tuff and post-caldera lavas. Ti-in-zircon thermometry shows that the Singkut magma body experienced a temperature increase starting approximately upon eruption of the pre-caldera lavas (~254 ka). Such thermal perturbation determined progressive melting of mineral phases in the cumulate crystal mush, caused the resorption of the youngest zircon domains before the caldera-forming eruption, and hampered zircon crystallization between the caldera-forming eruption and the effusion of the post-caldera lavas (~16 ka). Our data demonstrate how cumulate melting processes played a key role in leading the volcanic system towards a caldera-forming eruption and controlled the transitions in eruptive style between the effusive phases and the explosive climactic eruption.

1. Introduction

Caldera-forming eruptions represent the most violent expression of silicic volcanism on Earth.

Understanding the physico-chemical conditions that control the growth and storage of the large silicic reservoirs that feed these eruptions, and the timescales over which magma evolutionary processes operate, is a difficult task. Over the decades, petrological studies and geophysical investigations have significantly improved our understanding of the architecture and character of silicic magma reservoirs suggesting that magmas spend most of their life in a high-crystallinity state (e.g., Bachmann and Huber, 2016; Cooper and Kent, 2014; Edmonds et al., 2019; Ward et al., 2014). Zircon geochronology and thermal modeling have shed light into the longevity of such magmatic systems revealing that they can survive and evolve over timescales of hundreds of thousands of years (Bohrson and Reid, 1997; Karakas et al., 2017; Szymanowski et al., 2017; Townsend et al., 2019). Detailed geochemical analyses of erupted magmas have shown that crystal accumulation leading to the generation of cumulate crystal mushes and extraction of supernatant crystal-poor melts from their mushy counterpart, play a pivotal role in controlling the chemical evolution and growth of large silicic magma bodies in the upper crust (Hildreth, 1981;

Bacon and Druitt, 1988; Bachmann and Bergantz, 2004; Hildreth and Wilson, 2007; Cooper, 2017; Wolff et al., 2020). Injection of more mafic, hotter, and volatile-rich magmas of deeper origin can facilitate eruption of the crystal-poor and highly buoyant melts and exerts a major control on the eruptibility of the more crystalline and sluggish portions of magma reservoirs during large explosive eruptions (Sparks et al., 1977; Pallister et al., 1992; Wark et al., 2007; Molloy et al., 2008; Ellis et al., 2023). Such behavior has been described in great detail in ignimbrite sequences where compositional and crystallinity gradients are present and interpreted as the expression of zoned magma reservoirs progressively tapped during eruption, from a more evolved and crystal-poor top to a more mafic and crystalline bottom (Wolff and Storey, 1984; Wolff et al., 2015; Forni et al., 2016; Di Salvo et al., 2020; Foley et al., 2020; Keller et al., 2021). On the contrary, the mechanisms that control the defrosting of large monotonous crystal-rich magma bodies to produce caldera-forming eruptions are more elusive due to the remarkable compositional homogeneity of the erupted magmas that may mask subtle geochemical variations (Bachmann et al., 2005; Cooper and Wilson, 2014; Watts et al., 2016; Sliwinski et al., 2017; Repstock et al., 2018). Additionally, the time elapsed between cumulate mush reactivation and eruption in both zoned and monotonous reservoirs remains overall controversial with timescales ranging from centuries to hundreds of thousands of years (Burgisser and Bergantz, 2011; Matthews et al., 2012; Wotzlaw et al., 2013; Klemetti and Clynne, 2014; Tapster et al., 2016; Szymanowski et al., 2019). Such a knowledge gap makes interpretation of the signals of potential renewal of the volcanic activity at restless caldera-forming magmatic systems extremely challenging (e.g., Singer et al., 2014). To solve this conundrum, more case studies are needed where geochemical investigations aimed at fingerprinting cumulate melt processes are combined with geochronological data aimed at constraining their timescales and relationship with the eruptive activity.

In this paper, we focus on the Singkut caldera, a poorly studied Quaternary volcanic system from northern Sumatra (Indonesia). Singkut is located ~40 km southeast of the major city of Medan one of Indonesia's largest urban areas with a population of 3.4 million inhabitants (Fig. 1). Singkut mostly erupted crystal-rich lavas during the pre- and post-caldera phases of activity and a crystal-rich ignimbrite during a caldera-forming eruption. Hence, this magmatic system offers a unique opportunity to track the evolution of a highly crystalline magma reservoir progressing towards a caldera-forming eruption and recovering from the climactic event. In this paper, we utilize field observations to map the extension and thickness of the Singkut volcanic deposits and use these data to estimate the erupted volumes. We use major and trace element data of bulk-rock, glasses, and minerals to characterize the pre-eruptive conditions of pre- and post-caldera lavas and caldera-forming tuff, as well as ^{14}C and zircon (U–Th)/He geochronology to determine the eruption ages. In addition, a combination of in-situ LA-ICP-MS U–Pb and U–^{230}Th zircon dating, and Ti-in-zircon thermometry provides insight into the mechanisms that led to the Singkut caldera-forming eruption and those that controlled the post-caldera activity.

2. Geological setting

The island of Sumatra (Indonesia) is located in the Indian Ocean where it forms a ~ 1760 km-long and NW-SE-oriented feature, parallel to the westernmost sector of the Sunda trench. The formation of the Sunda trench is related to the subduction of the Indo-Australian oceanic plate underneath the Eurasian continental plate (Hamilton, 1979) with a convergence rate of ~5–7 cm/yr (Prawirodirdjo et al., 2000). Due to the NNE movement of the Australian-Indian plate, subduction is perpendicular to the trench in the south of Indonesia (Java) and oblique in the west (Sumatra) where kinematics are mechanically compensated by strike-slip deformation along the Sumatran Fault Zone (SFZ) (McCaffrey, 1991; McCaffrey et al., 2000). The SFZ is a NW-SE-trending, dextral strike-slip fault system, which extends across the whole length of Sumatra delineating an array of Quaternary volcanoes and calderas (Fig. 1). Throughout the central and most of southern Sumatra, the active volcanic arc is located within ~50 km of the SFZ, but in the northern sector the location of the volcanic centres is shifted to the east due to a change of the angle of subduction in the area, where the trench intersects the Investigator Fracture Zone (IFZ) (Fauzi et al., 1996) (Fig. 1). According to some authors (e.g., Koulakov et al., 2016), this peculiar geodynamic setting might represent the main cause for the exceptionally vigorous volcanic activity at Toba, where at least four large caldera-forming eruptions have occurred over the last ~1.4 My (Chesner and Rose, 1991; Chesner, 1998). The latest of these eruptions, the Youngest Toba Tuff (YTT, ~74 ka), represents the largest known Quaternary caldera-forming eruption (Rose and Chesner, 1987; Chesner et al., 1991; Costa et al., 2014; Mark et al., 2014; Szymanowski et al., 2023). Although Sumatra is mostly known for hosting the Toba caldera, the occurrence of widespread and thick proximal pyroclastic sequences on the island (Westerveld, 1952), together with the presence of abundant tephra layers of Sumatran origin in the distal marine stratigraphic record (Ninkovich et al., 1978; Salisbury et al., 2012; Bouvet de Maisonneuve and Bergal-Kuvikas, 2020; Kutterolf et al., 2023), suggest that Sumatra might have produced a much greater number of large eruptions, many of which have so far received little attention. In this paper, we provide the first volcanological and petrological characterization of one of these poorly studied magmatic systems from northern Sumatra: the Singkut caldera.

3. Field data

3.1. Singkut caldera

Singkut is a ~ 9 km wide caldera located ~35 km north of Toba and ~ 15 km to the north-east of the active Sinabung volcano (Fig. 1). The caldera is delimited to the south and southeast by ~300 m-high cliffs where pre-caldera lavas are exposed (Fig. 2a). A partially eroded pre-caldera edifice, Mt. Simpulangin, is located in the north-eastern flank of the collapsed structure while the inner part of the caldera is occupied by three younger post-caldera volcanoes aligned on a SE-NW trend (Mt.
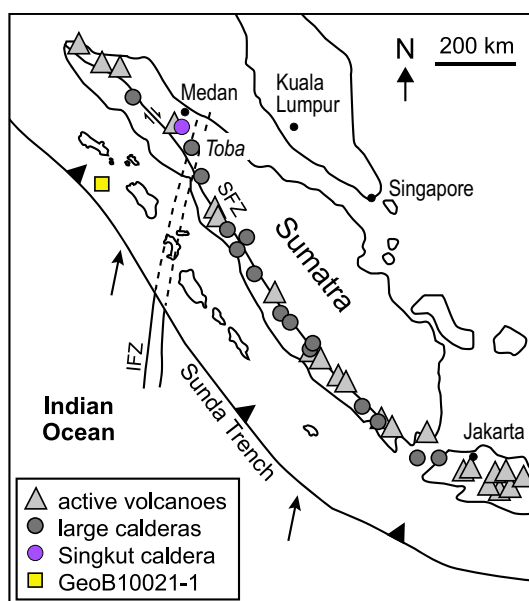

Fig. 1. Sketch map showing the location of large calderas and active volcanoes on Sumatra (Whelley et al., 2015) as well as the position of the Toba caldera relative to the continuation of the Investigator Fracture Zone (IFZ) and the Sumatran Fault Zone (SFZ). The location of the Singkut caldera together with that of the marine core GeoB10021–1 (RV SONNE CRUISE SO-184; Hebbeln, 2006) are highlighted using color-coded symbols.
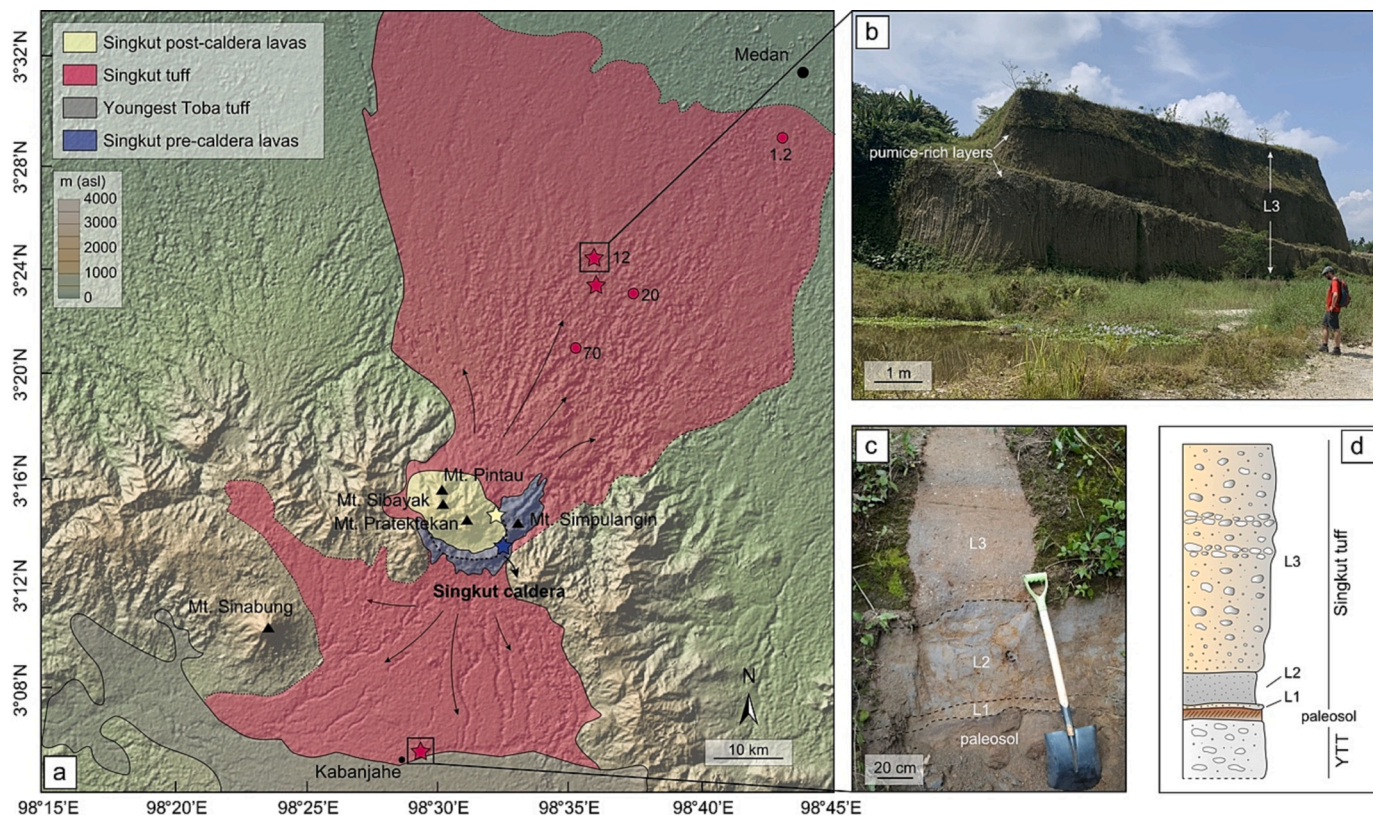
Fig. 2. Map of the Singkut area showing the extension of the Singkut caldera, the distribution of the pre- and post-caldera lavas, and the Singkut tuff pyroclastic deposits (after Cameron et al., 1982). Star symbols indicate the sampling locations while dots indicate the location of the studied outcrops with numbers referring to the thickness of the pyroclastic deposits. The area surrounding the Singkut caldera and its deposits is characterized by the occurrence of andesitic to dacitic lavas and pyroclastics of Plio-Pleistocene age, likely forming a widely distributed volcanic field (elevated morphologies on the map; Cameron et al., 1982) (a). Field photos showing a typical outcrop of the L3 subunit with the pumice-rich layers (b) and the base of the Singkut tuff (subunits L1, L2, and the base of L3) above a paleosol close to the village of Kabanjahe (c). Schematic stratigraphic column showing the relationship between the Singkut tuff and the Youngest Toba Tuff (YTT) (d).

Pratektekan, Mt. Sibayak, and Mt. Pintau; Fig. 2a) and hosts an active geothermal field (Daud, 2001). Information about the volcanological and geochronological evolution of the Singkut volcanic complex is extremely poor. The last eruption is believed to have occurred in 1881 CE (Van Padang, 1983) and was presumably sourced from the twin cones of Pintau and Sibayak. Detailed information about the eruptive style and magnitude of this eruption is not available, but the presence of a 900 m-wide summit crater at Sibayak indicates that the most recent activity of the Singkut complex was likely explosive. A thick pyroclastic sequence (hereafter named "Singkut tuff") was recognized within a vast area to the north and south of the Singkut caldera. The Singkut tuff extends up to ~40 km to the north where it reaches the city of Medan, and ~20 km to the south of the caldera. The deposits reach up to 70 m in thickness ~15 km to the north of the caldera and decrease down to 1.2 m at a distance of ~35 km from the centre of the caldera (Fig. 2a,b). The Singkut tuff represents the only pyroclastic deposit that consistently crops out in the region between the cities of Medan and Kabanjahe (Fig. 2a,b). The thickness of the Singkut tuff decreases with the distance from the caldera (Fig. 2a) and pyroclastic deposits with similar characteristics make up the ~500 m-thick caldera infill (Atmojo et al., 2000). Based on these features, we unequivocally identify the Singkut caldera as the source of this ignimbrite.

The Singkut tuff is a complex pyroclastic sequence composed of three main subunits defined based on vertical variations of the textural characteristics of the deposits. From bottom to top we distinguished an 8 cm-thick, clast-supported, well-sorted, beige angular pumice layer (L1) overlaid by a 50 cm-thick layer composed of gray ash with scattered

white pumices and abundant organic material (L2), above which the main unit (L3) occurs (Fig. 2c,d). The base of L3 is a matrix supported deposit showing some crude layering and composed of beige and gray ash with scattered white pumices. L3 abruptly transitions into a massive deposit showing a higher concentration of white and gray angular to sub-angular pumices (up to 40 cm) and lithic clasts (up to 20 cm) in a coarse ash matrix. Several pumice-rich layers varying in thickness between ~1 and 2 m occur at different stratigraphic heights, likely separating different depositional units (Fig. 2b). In the most distal outcrops (~35 km to the north of the caldera), L3 is a ~1.2 m-thick, cross-bedded and fine ash deposit with lenses of cm-sized pumices (exceptionally up to 20 cm in diameter). The base of the Singkut tuff was identified in a river valley located close to the village of Kabanjahe (~14 km to south of the caldera) where a well-developed paleosol is exposed below L1 (Fig. 2a, c). In this area, the paleosol separates the Singkut tuff from the YTT pyroclastic deposits. This observation places important constraints on the relative age of the Singkut tuff which must be younger than 74 ka (i. e., ^{40}Ar/^{39}Ar age of sanidines from YTT; Mark et al., 2017).

A distal tephra layer correlated with the Singkut tuff based on its geochemical signature (Fig. S1; Phua, 2022) has been identified in the marine core GeoB10021–1 (R/V SONNE CRUISE SO-184; Hebbeln, 2006) collected using a gravity corer from a small basin located to the northwest of Nias island, offshore of north Sumatra (Fig. 1). The ash bed is identified at the sediment core interval between 118 and 119 cm below the sea floor and consists of visible ash pod about 2 cm thick and 4 cm wide, composed of gray fine ash with abundant clear and colorless glass shards.

3.2. Sampling

The pre-caldera lavas (SKT-19-10) were collected on the southeastern caldera rim (Fig. 2a). Juvenile clasts from the Singkut tuff were sampled at different stratigraphic heights from the outflow deposits to the north and south of the Singkut caldera. White pumices from subunits L1, L2, and the base of L3 were sampled close to Kabanjahe, ~14 km to the south of the caldera (SKT-20-10C, SKT-20-10D, and SKT-20-20E, respectively) (Fig. 2a). Organic material was collected from L2 (Fig. 2c) for radiocarbon dating. White and gray pumices from the upper part of L3 were sampled below (SKT-19-01 and SKT-19-02), within (SKT-19-03 and SKT-19-04), and above (SKT-19-05 to SKT-19-07) the lowermost visible pumice-rich layer (Fig. 2a,b). Post-caldera lavas (SKT-19-09) were sampled from the northeastern flank of Mt. Pratektekan inside the Singkut caldera (Fig. 2a). Sampling of fresh rocks from the other post-caldera volcanoes was not possible due to the high degree of hydrothermal alteration of the deposits. Overall sampling was extremely challenging due to the thick vegetation cover and difficulty in accessing the inner part of the caldera. Sample description and sampling locations are provided in the Supplementary Table 1.

4. Analytical methods

4.1. Crystallinity

The crystallinities of single juvenile clasts from L1, L2, and L3 (white and gray pumices) were estimated using the method of Rowe et al. (2012). Powder samples were analyzed at the Nanyang Technological University (NTU, Singapore) using a Panalytical X'Pert pro X-ray diffractomer (XRD) with a Cu-Kα radiation source operated at 40 kV and 30 mA and equipped with a X'Celerator 1D type detector. The crystallinities of the pre- and post-caldera lava samples were determined using backscattered electron (BSE) maps and images taken with a JEOL JSM-7800F field emission Scanning Electron Microscope (SEM) at NTU (Singapore). Following the method of Bernard et al. (2022), image thresholding using JMicrovision v1.3.1 (Roduit, 2007) in combination with manual outlining of crystals was used to estimate the microphenocryst and phenocryst (crystals >100 μm in length) fractions. This framework was preferred to the method of Rowe et al. (2012) used for pumices to avoid including groundmass microlites in the crystallinity calculation, given that microlites likely crystallized outside of the storage zone. The crystallinity calculations and analytical conditions are reported in the Supplementary Table 1.

4.2. Major and trace element data

The pre- and post-caldera lavas and pumices from the Singkut tuff were analyzed via ICP (major elements) and ICP-MS (trace elements), after being crushed and fused with lithium metaborate and tetraborate at the Actlabs laboratories (Ancaster, Ontario). Glass major and trace elements compositions were acquired for representative samples of all the subunits of the Singkut ignimbrite (L1–L3), whereas mineral compositions (plagioclase, amphibole, pyroxene, biotite, and Fe–Ti oxides) were obtained for the lava samples too. The major element compositions of glass and minerals were obtained at NTU (Singapore) using a Jeol JXA-8530F field emission electron probe X-ray microanalyzer (EPMA). Acceleration voltage was set to 15 kV for all our analyses, but different probe currents and beam sizes were used for matrix glasses and amphibole-hosted melt inclusions (6 nA and 10 μm), plagioclase (10 nA and 5 μm), pyroxene and Fe–Ti oxides (20 nA and focused beam), amphiboles (10 nA and 5 μm) and biotites (10 nA and 20 μm). To minimize alkali migration, K and Na were always analyzed first. Secondary standards for glass and mineral analyses were frequently measured to ensure analytical stability. Data are reported in the Supplementary Table 1.

4.3. In-situ U–Pb and U–Th zircon dating and trace elements

All in situ U–Pb and ^{230}Th–^{238}U analyses of zircon, ^{230}Th–^{238}U analyses of glass, and trace element analyses of glass, zircon, amphibole, plagioclase, and Fe–Ti oxides were carried out at ASE, NTU (Singapore) using a Teledyne (Photon Machines) Analyte G2 laser ablation system coupled to a Thermo Scientific Element 2 ICP-MS. All trace element and geochronological data are reported in Supplementary Tables 1 and 2, respectively. Details of the analytical procedures for each method are listed in Supplementary Table 3.

The Trace Elements IS DRS in Iolite v. 3.6 was used for data reduction of trace element analyses of all phases. For glass, NIST SRM 612 was used as the primary calibration standard, and GSD-1G was used for calibrating the silicate and oxide minerals. The Si content of glass and silicates determined by EPMA and the Ti content of Fe–Ti oxides determined by EPMA were used as the internal standards. Glass trace element compositions were further corrected for interelement fractionation (matrix mismatch) using correction factors determined by measurements of ATHO-G, T1-G, and BCR-2G following the suggestions of Pearce et al. (2011). Reproducibility of trace element analyses was better than 10% (2σ) for all elements with concentrations >1 ppm.

Zircons were hand-picked from the heavy and diamagnetic fraction (< 250 μm) and mounted in epoxy. Cathodoluminescence (CL) images of the zircon crystals were obtained at NTU (Singapore) using a JEOL JXA-8530F field emission electron probe X-ray microanalyzer (EPMA) equipped with a JEOL cathodoluminescence (CL) detector. A focused beam with an acceleration voltage of 15 kV and current of 5 nA was used for imaging. 1048 × 1048 pixels CL maps were acquired with a dwell time of 6 ms.

Zircon U–Pb data were reduced with the U–Pb Geochronology data reduction scheme (DRS; Paton et al., 2010) of Iolite v. 4 (Paton et al., 2011) using 91,500 zircon as the primary calibration standard. For initial U–Th disequilibrium and common Pb corrections, we utilized the DQPB software (Pollard et al., 2023). Precision and accuracy on U–Pb dates based on reference materials analyzed as unknowns are 1.0–1.5% (2σ) and better than 2.5%, respectively. Precision related to the common Pb and disequilibrium correction is propagated using a Monte Carlo approach with DQPB.

Zircon trace element concentrations and isotopes for U–^{230}Th dating were collected simultaneously, and the same intervals were selected for processing both. Trace element data were reduced using the methods described above for the other silicate minerals. Iolite v. 4 was used for interval selection and gas blank subtraction of ^{238}U–^{230}Th analyses of zircon and glass. Further data reduction was carried out using an Excel spreadsheet following the methods of Guillong et al. (2016). Correction factors for instrument drift, zirconium oxide interference, mass bias, and interelement fractionation were determined using 91,500 zircon and NIST SRM 612 for zircon and glass, respectively, and a natural monazite crystal was used for determining the abundance sensitivity correction factor for ^{232}Th on ^{230}Th. A set of in-house and international reference zircons with ages >900 ka were used to check that the data reduction routine resulted in U–Th isotopic ratios indicative of secular equilibrium for sufficiently old zircons. U–Th model ages of individual zircon grains were calculated in two different ways: 1) using the matrix glass composition to infer the $(^{230}Th/^{232}Th)_0$ assuming equilibrium between zircon and melt ("two point zircon-glass isochron"; Reid et al., 1997) and 2) using the approach of Boehnke et al. (2016) to model the $(^{230}Th/^{232}Th)_{magma}$ for each zircon assuming a U and Th zircon/melt partition coefficient, and subsequently calculate individual zircon ages using the two point isochron. For the U–Th ages, where the 2σ uncertainties are comparable to the maximum age difference, weighted mean and isochron ages were calculated. Zircons from the Campanian Ignimbrite syenitic ejecta (Breccia Museo unit, BM; Fedele et al., 2008), for which a LA-ICP-MS U–Th isochron age of 42.1 ± 1.8 ka is reported in Guillong et al. (2016), were treated as unknowns to validate precision and accuracy. Reproducibility of BM zircons analyzed as unknowns
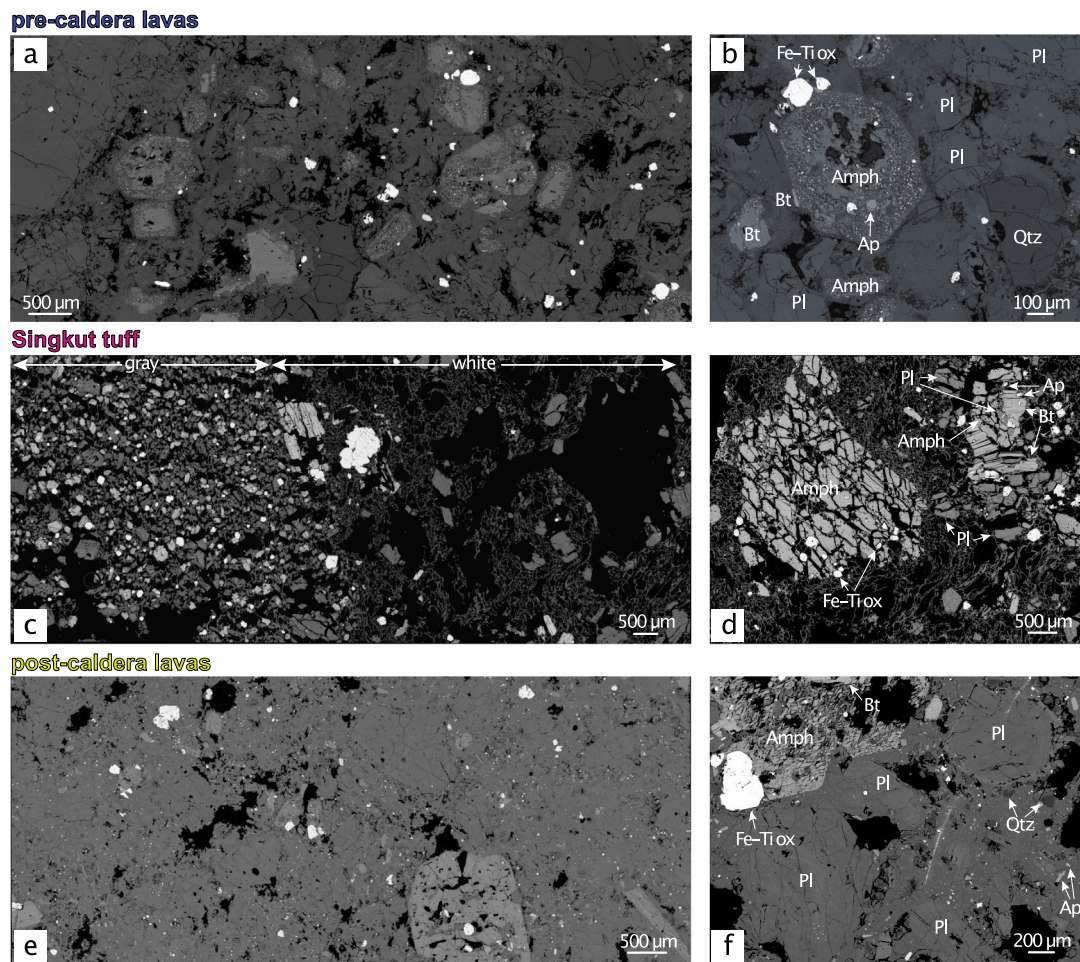
Fig. 4. Variation of the crystallinity (vol% crystals) in the studied units arranged according to their stratigraphic height. W = white pumices; G = gray pumices.

ranged from 10 to 15% (2σ). The ages calculated for the BM zircon using both methods described above overlap with the reported age given the analytical uncertainty. However, method 2 resulted in a more accurate result (see Supplementary Table 2).

4.4. (U–Th)/He dating

(U–Th)/He zircon ages were obtained using the method described in detail in Danišík et al. (2017). Zircons were selected based on their size (>60 μm on the short axis) and aspect (i.e., inclusion- and imperfection-free, euhedral, unaltered clear crystals), hand-picked, and leached in concentrated HF for ~1 min to remove the adherent glass. The most suitable crystals were photographed and measured using a stereo microscope connected to a camera then mounted on a double-sided tape for LA-ICP-MS depth profile analyses. Rim-to-core U and Th distribution as well as U–Pb and/or U–^{230}Th ages were measured using a Resonetics Resolution 155, 193 nm Ar–F excimer laser ablation system coupled to a Thermo-Scientific ElementXR ICP-MS at ETH Zurich (Switzerland). The operating conditions were the following: 40 × 40 μm spot size, 10 Hz repetition rate, 2.0 J/cm^3 fluence, 20 s ablation time, and 30 s gas blank acquisition. Zircon crystals were then packed in Nb foil, loaded in a ultrahigh vacuum line to determine ^{4}He abundance for each grain. Helium was extracted from the zircons by heating with a diode laser equipped with a pyrometer for temperture stabilisation in the range of 1100 °C for 45 min, and the released gas was analyzed with a static-vacuum magnet sector-field noble gas mass spectrometer equipped with a GS98 Baur-Signer ion source at ETH Zurich. Several re-extractions at progressively higher temperatures were performed until

the fraction of helium from the last extraction was <1% of the total. The measured helium for each grain was corrected for the blank measured using empty Nb wraps. Outgassed zircons were transferred into Teflon vials, spiked with ^{236}U and ^{230}Th, and dissolved using HF, HNO$_3$, and HCl acids. Solutions were then analyzed for U and Th using an ElementXR ICP-MS. "Raw ages" were calculated using the He, U, and Th abundances and uncertainties derived from the propagated analytical uncertainties of each measurement. "Raw ages" were corrected for He loss due to alpha-ejection ("FtK-corrected (U-Th)/He ages") and core-to-rim U–Th zoning ("FtZ-corrected (U-Th)/He ages") using the methods of Ketcham et al. (2011) and Hourigan et al. (2005) and subsequently for disequilibrium ("disequilibrium-corrected (U-Th)/He ages") using the MCHeCalc computational routine (Schmitt et al., 2010). As input parameters we used single crystal Ftz-corrected (U–Th)/He ages and the U–Pb or U–^{230}Th crystallization ages with 2σ uncertainty. Zircons from the Fish Canyon Tuff ((U–Th)/He age of 28.3 ± 0.8 Ma, 2σ uncertainty; Gleadow et al., 2015) and from the Breccia Museo unit of the Campanian Ignimbrite ((U–Th)/He age of 41.7 ± 1.8 ka, 2σ uncertainty; Gebauer et al., 2014) were measured to monitor accuracy, analytical stability, and goodness of the various corrections. The analytical data and results are reported in the Supplementary Table 2.

4.5. Radiocarbon dating

Organic-rich material sampled onshore within the L2 unit of the Singkut tuff (Fig. 2c), as well as foraminifera sampled offshore from the sediment interval (117–118 cm) directly above the volcanic ash layer correlated to the Singkut tuff within marine core GeoB10021–1 were
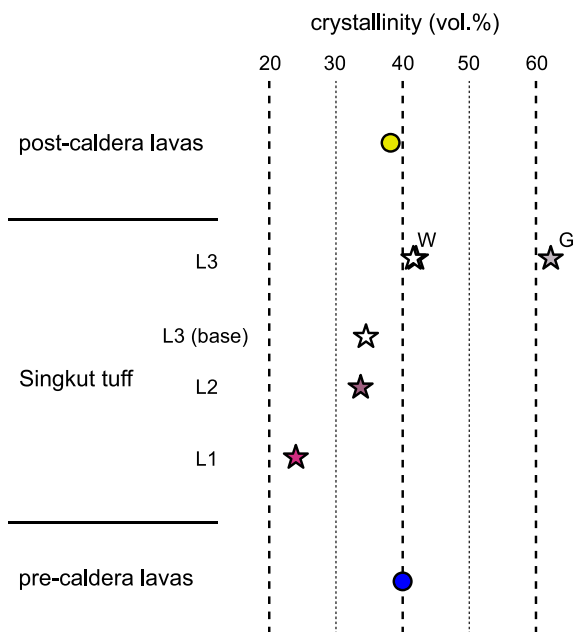
Fig. 3. Back-scattered electron images (BSE) of selected samples from pre-caldera lavas (a-b), a white and gray pumice from the Singkut tuff (c-d), and the post-caldera lavas (e-f) showing textures and typical mineralogy (Pl = plagioclase; Amph = amphibole; Qtz = quartz; Bt = biotite; Fe–Ti ox = Fe-Ti oxides; Ap = apatite). Note that resorbed quartz crystals are abundant in pre-caldera lavas and scarce in the Singkut tuff and post-caldera lavas.

analyzed with the radiocarbon dating method. Radiocarbon measurements were performed by accelerator mass spectrometry (AMS) at the Beta Analytic Radiocarbon Laboratory (USA). Radiocarbon dating results are reported both as conventional ages (^{14}C yr BP) with 2σ uncertainty and as calibrated ages (cal a BP) in the form of median ages, 68.2% (1σ) and 95.4% (2σ) probability calibrated age ranges (Supplementary Table 2). Conventional radiocarbon ages (^{14}C yr BP) were calibrated with MatCal 2.0 (Lougheed and Obrochta, 2016) using the IntCal20 calibration curve (Reimer et al., 2020) for the onshore organic-rich clay clasts, and the Marine20 (Grootes et al., 2020) calibration curve for the offshore foraminifera with an additional ΔR correction of -117 ± 70 (Southon et al., 2002) to account for the marine radiocarbon reservoir effect. A weighted-mean age for the tephra layer was calculated using IsoplotR (Vermeesch, 2018; see Supplementary Table 2).

5. Results

5.1. Mineralogy and crystallinity of lavas and pumices

The pre-caldera lavas from Singkut are coarse-grained with 40 vol% crystals (>100 μm) of plagioclase, amphibole, biotite, orthopyroxene, Fe–Ti oxides, quartz, apatite, and zircon in a micro- to crypto-crystalline groundmass (Figs. 3a,b, 4 and S2). The juvenile clasts from the Singkut tuff are white and gray pumices occurring both as single clasts and as portions within the same clast (Fig. 3c). White pumices prevail at the bottom of the sequence (L1), while gray clasts/portions become abundant in the main ignimbrite body (L3). The crystallinity of white pumices/portions changes from 24 vol% in L1 to 34 vol% in L2 and ranges between 35 and 42 vol% crystals in L3, while the gray pumices/portions in L3 contain between 42 and 62 vol% crystals (Fig. 4). The mineral assemblage is very similar to that observed in the pre-caldera lavas, but quartz is rare (Figs. 3c and S2). Crystals in both white and gray pumices/portions are often broken and immersed in a glassy vesicular matrix (Figs. 3c,d and S2). The post-caldera lavas from Pratektekan volcano are very similar to the pre-caldera lavas in terms of texture and mineralogy with slightly lower crystallinity (38 vol% crystals >100 μm; Fig. 4).
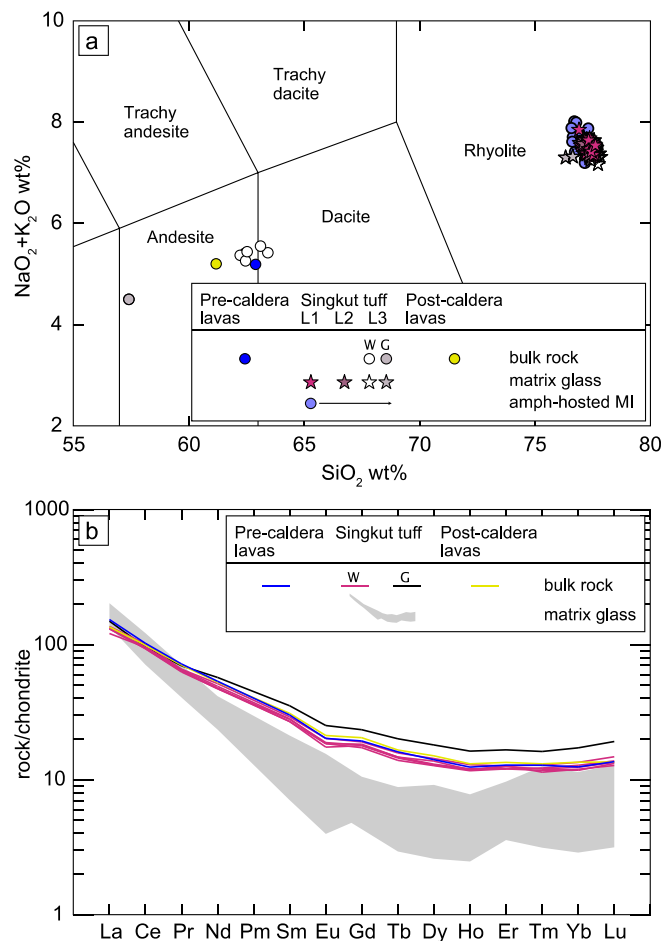

Fig. 5. Total alkali vs. SiO$_2$ classification diagram (TAS; Le Bas et al., 1986) showing the bulk-rock, melt inclusion and matrix glass compositions of pyroclastic rocks and lavas from Singkut (a). Rare Earth Element (REE) patterns of bulk-rock and matrix glass compositions from Singkut showing depletion in MREE in the matrix glasses compared to the bulk-rocks (b). Data normalized to chondrites from McDonough and Sun (1995). W = white pumices; G = gray pumices.

Notably, they contain only traces of quartz in the micro-crystalline groundmass (Figs. 3e,f and S2). Crystal clots containing amphibole, biotite, plagioclase, and oxides are very common in both lavas and pumices (Figs. 3 and S2).

5.2. Bulk-rock and glass compositions

The bulk-rock composition of pre-caldera lavas plots at the limit between the andesite and dacite fields, whereas the post-caldera lavas plot within the andesite field (Fig. 5a). The juvenile clasts from the Singkut tuff range in whole-rock composition from low-SiO$_2$ andesites (gray pumice) to high-SiO$_2$ andesites and dacites (white pumices) but the matrix glass of both white and gray pumices/portions is rhyolitic (Fig. 5a).

Major element plots show a decrease in Al$_2$O$_3$, TiO$_2$, CaO, FeO, and MgO, and an increase in K$_2$O with SiO$_2$ from basaltic andesite to andesite bulk-rock compositions, whereas Na$_2$O displays little variation (Figs. 6a–c and S3). The bulk-rock compositions of the white pumices and pre-caldera lavas are similar. The post-caldera lavas have slightly higher TiO$_2$, CaO, MgO, and FeO, and lower SiO$_2$ and K$_2$O, while the gray pumices are significantly enriched in all major elements except for SiO$_2$, Na$_2$O, and K$_2$O compared to the other bulk-rock compositions (Figs. 6a–c and S3). In the rhyolitic matrix glasses, CaO, MgO, FeO, P$_2$O$_5$, and Al$_2$O$_3$ contents are homogeneously low, while Na$_2$O and TiO$_2$
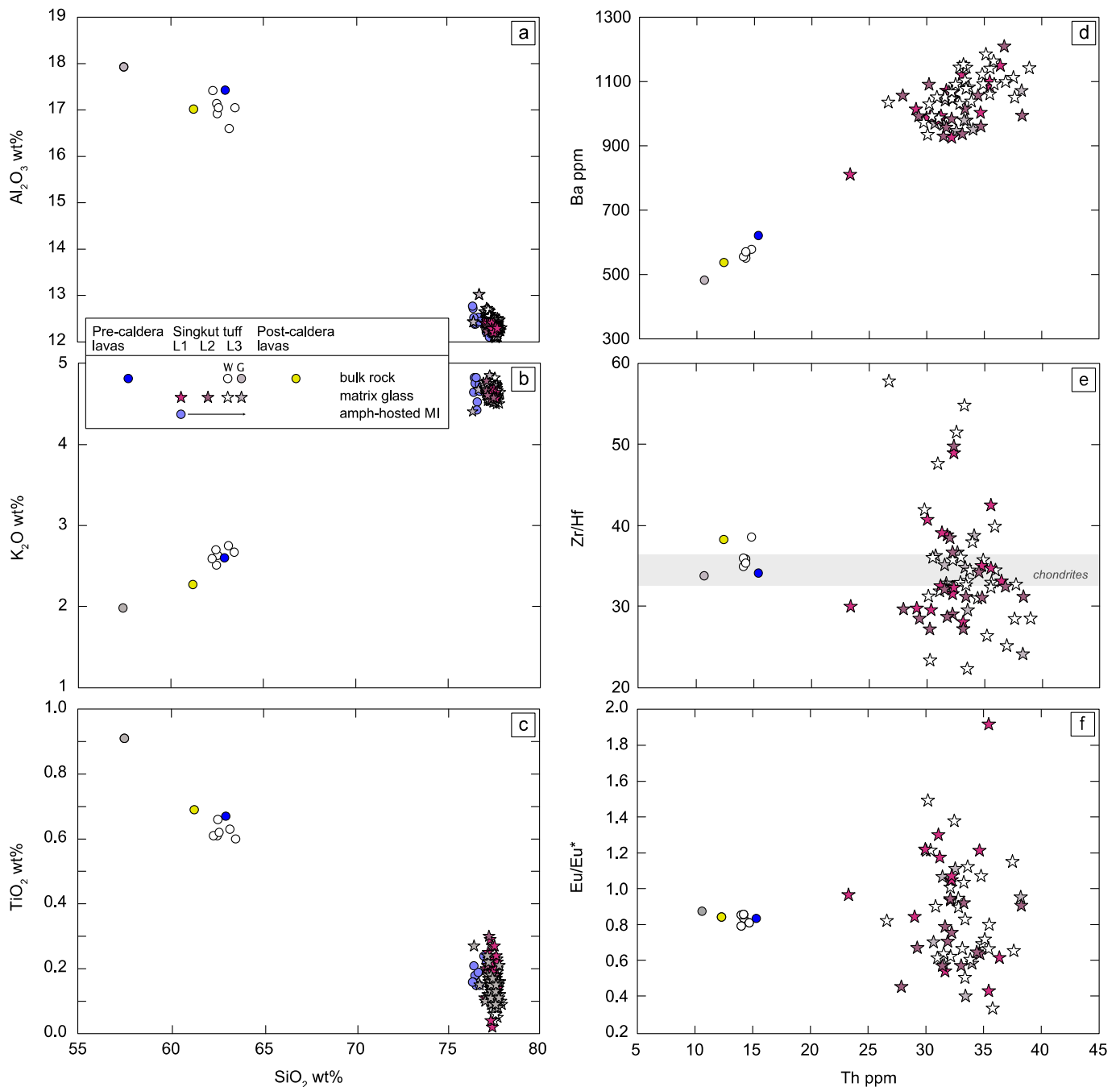
Fig. 6. Selected binary plots of major (a-c) and trace elements (d-f) showing the compositional variations displayed by Singkut lavas and pyroclastics. Eu/Eu* = Eu$_N$/(Gd$_N$*Sm$_N$)$^{1/2}$, data normalized to chondrites from McDonough and Sun (1995). W = white pumices; G = gray pumices.

show wider variations over relatively homogeneous SiO$_2$ contents (Figs. 6a–c and S3).

Amphibole-hosted melt inclusions from the Singkut tuff mostly overlap with matrix glass compositions (Figs. 6a–c and S3). Rare earth element patterns show notable depletion in middle REE (MREE) over light REE (LREE) and heavy REE (HREE) in the matrix glasses compared to bulk-rock compositions. The gray pumice bulk-rock composition is enriched in MREE and HREE compared to the white pumices and lavas (Fig. 5b). Trace element binary plots display small differences between the bulk-rock compositions of pre-caldera lavas and white pumices, while the gray pumices show lower Th and Ba contents (Fig. 6d–f). The post-caldera lavas mostly plot halfway between the two. The rhyolitic matrix glasses are enriched in Th and Ba compared to the bulk-rock compositions and show wide variations in Eu/Eu* (=Eu$_N$/

(Gd$_N$*Sm$_N$)$^{1/2}$; 0.4–1.2) and Zr/Hf (22–48) (Fig. 6d–f). Overall, no significant compositional difference is observed between the matrix glass compositions of white and gray pumices.

5.3. Mineral chemistry

5.3.1. Plagioclase

Plagioclase crystals are generally euhedral and display a wide range of crystal sizes (from ~0.3 mm to 2.5 mm) and compositions (An$_{30–86}$). The plagioclase from the pre- and post-caldera lavas and Singkut tuff show similar compositional and textural features and are often included within amphibole crystals or form crystal clots together with amphibole, biotite, Fe–Ti oxides, and apatite (Fig. 3). Most plagioclase crystals have labradoritic composition, while bytownite is rare, often representing
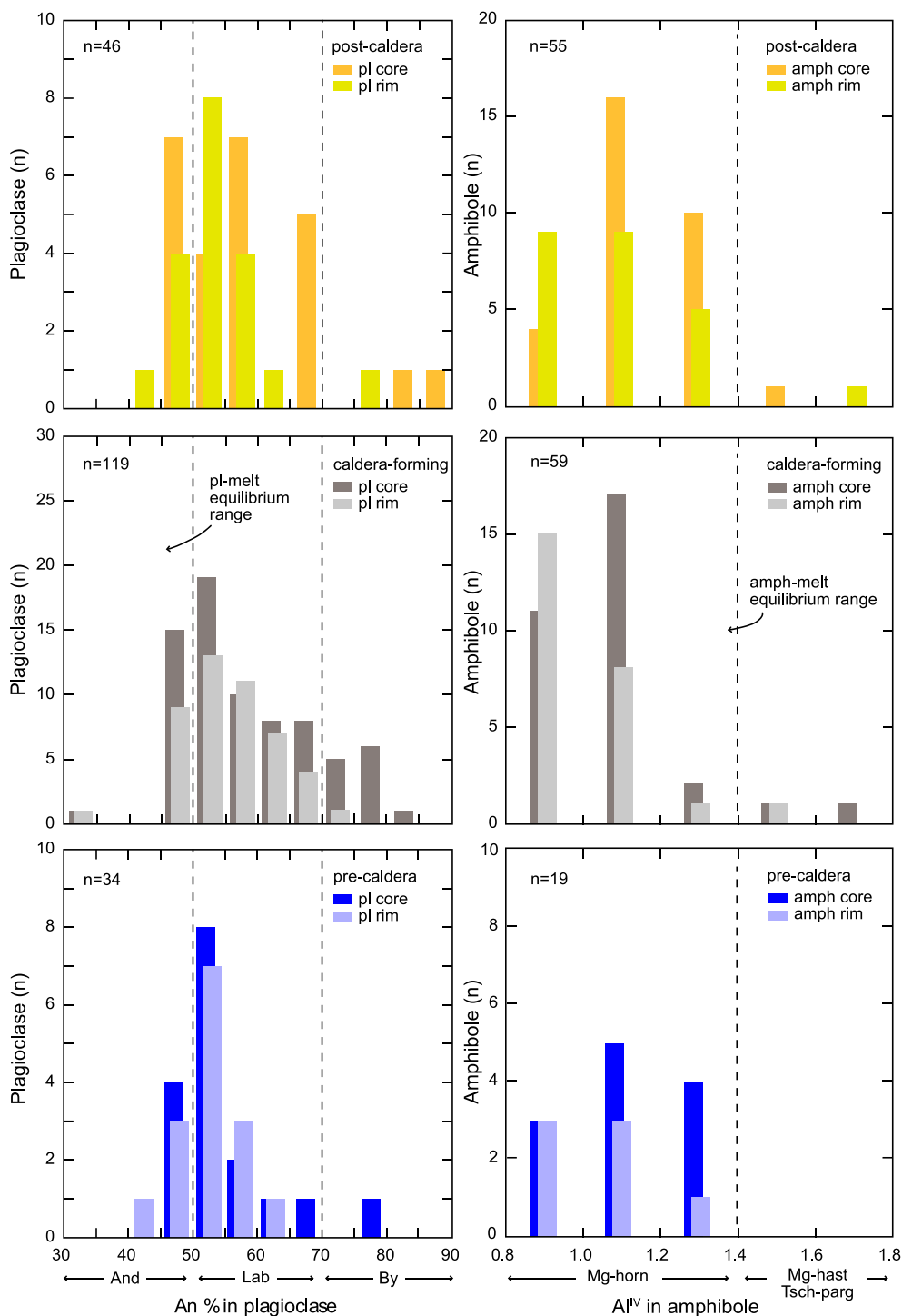
Fig. 7. Histograms showing the variation of anorthite content (An%) in plagioclase (a–c) and of Al in the T site (Al^{IV}) in amphiboles (d–f) from the pre- and post-caldera lavas and the Singkut tuff. Gray shaded areas indicate the compositional fields where minerals are in equilibrium with the melt (represented by the matrix glass compositions) in the Singkut tuff. Plagioclase-melt and amphibole-melt equilibrium relationships were investigated using the equilibrium tests of Putirka (2008) and Putirka (2016), respectively.

crystal cores of oscillatory or patchy zoned crystals with labradorite to andesine intermediate and outermost rims (Fig. 7a–c). Only in the Singkut tuff, rare small subhedral low-Ca plagioclase (An$_{30–31}$) have been observed (Fig. 7b). In most plagioclase, the An content positively correlates with FeO while no clear correlation between the An content and the Sr and Ba contents has been observed (Fig. S4).

5.3.2. Amphiboles

Amphibole crystals are euhedral to subhedral, often shattered and range in size between 0.1 and 2 mm (Fig. 3). In the pre-caldera lavas, the amphiboles show breakdown rims composed of Fe–Ti oxides and plagioclase (Fig. 3a,b). Most amphiboles in both lavas and pyroclastics are Mg-hornblende with Al^{IV} = 0.8–1.3 and Mg# = 57–70 (Fig. 7d–f). Tschermakite-pargasite and Mg-hastingsite (Al^{IV} = 1.4–1.7 and Mg# = 58–71) compositions are occasionally present only in the Singkut tuff
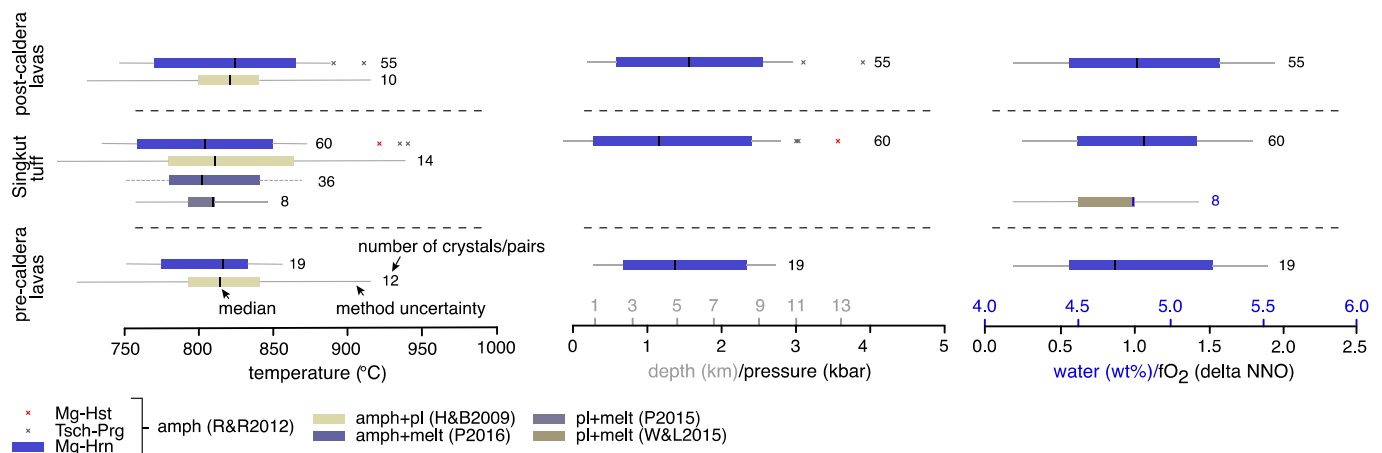
Fig. 8. Summary of the intensive parameters estimated using the following calibrations: pl + melt (P2008; Putirka, 2008), amph+melt (P2016; Putirka, 2016) and amph+pl (H&B1994; Holland and Blundy, 1994) thermometers, amphibole thermometers, and barometers (R&R2012; Ridolfi and Renzulli, 2012), and pl + melt hygrometer (W&L2015; Waters and Lange, 2015). Pl + melt and amph+melt equilibrium relationships were investigated using the equilibrium test of Putirka (2008) and Putirka (2016), respectively, whereas mineral-mineral equilibrium relationships for amph-pl pairs were inferred based on textural relationships (i.e., full contact between mineral pairs). Horizontal color-coded bars indicate the full ranges of estimated parameters with the median value, associated uncertainties and numbers of mineral or equilibrium mineral-melt pairs utilized for calculations. Pressures calculated using a crust density of 2800 km/m³. Pl = plagioclase; amph = amphibole; Mg-Hst = Mg-hastingsite; Tsch-Prg = Tschermakitic pargasite; Mg-Hrn = Mg-hornblende.

and in the post-caldera lavas (Fig. 7). The REE patterns of Mg-hornblende amphiboles fully overlap with small differences in Eu/Eu* that positively correlate with the Sr content. Overall amphiboles are enriched in MREE compared to HREE (Fig. S4).

5.3.3. Biotite

Biotite crystals are large (~1–1.5 mm), euhedral to subhedral, and frequently grow around crystal clots together with amphibole, plagioclase, and apatite (Fig. 3d,f). In the pre-caldera lavas, biotite crystals always display opacitic rims (Fig. 3a,b) while in the Singkut tuff they often appear frayed and deformed but fresh (Fig. 3c,d). Most biotites in the Singkut tuff have relatively low analytical totals (<95 wt%; definition of Ellis et al., 2022), and show higher CaO and lower K_2O, Na_2O, BaO, and MnO contents compared to those from the lavas (Fig. S5). Notably, in a K_2O vs. CaO space, biotites from L1, L2, and the base of L3 plot on a different trend compared to those from the rest of L3 (Fig. S5).

5.3.4. Fe–Ti oxides

Fe–Ti oxides in the Singkut tuff occur as single crystals or in crystal clots containing Ti-magnetite ($Usp_{0.17-0.19}$) and ilmenite ($Ilm_{0.74-0.80}$) with or without amphibole, biotite, apatite, and zircon. In all the lavas, Ti-magnetite crystals exhibit ilmenite lamellae indicative of exsolution-oxidation processes occurring at subsolidus temperatures (Bacon and Hirschmann, 1988).

5.3.5. Zircon

Zircon crystals are abundant in the pre-caldera lavas and scarcer in the Singkut tuff and post-caldera lavas where they often show signs of resorption (Fig. S6). CL images reveal zoning with rare evidence of inherited cores (Fig. S6). The Ti content corrected to the zircon reference material compositions of Szymanowski et al. (2018) varies between 3 and 9 ppm in zircons from the pre-caldera lavas, 3 and 29 ppm in zircons from the Singkut tuff and 3 and 28 ppm in zircons from the post-caldera lavas (Supplementary Table 1).

5.3.6. Other phases

Orthopyroxene crystals (50–60 μm) are overall scarce in lavas and pumices from Singkut. Mg-numbers mostly range between 64 and 68 but a few crystals with higher Mg-number (Mg# = 70–76) are present in both Singkut tuff and post-caldera lavas (Supplementary Table 1). Apatite is very abundant in both lavas and pyroclastics, often included in

other phases or mineral clusters (Fig. 3). Notably, rounded and embayed quartz (0.5–1 mm) is abundant in the pre-caldera lavas, scarce in the Singkut tuff and only present in traces within the post-caldera lavas (Fig. 3).

5.4. Intensive parameters

Magma storage conditions in terms of temperature, pressure, oxygen fugacity, and magma water content were estimated using a variety of thermometers, barometers, oxybarometers, and hygrometers and are summarised in Fig. 8. Temperature and pressure constraints using amphibole and amphibole-plagioclase thermobarometry were obtained for all the studied units, whereas the methods that require mineral-melt equilibrium (plagioclase-melt, amphibole-melt, and zircon saturation temperatures) were applied only to the Singkut tuff where the matrix, which quenched upon eruption, preserved a fully glassy texture and composition that likely approximates to that of the melt at the time of eruption (Fig. 3b). Amphibole and amphibole-plagioclase thermometry show similar temperature ranges in the pre-caldera lavas (~770–830 °C and ~ 790–840 °C, respectively), the Singkut tuff (~750–850 °C and 780–860 °C, respectively), and post-caldera lavas (~760–860 °C and ~ 800–840 °C, respectively; Fig. 8). Tschermakitic pargasite and Mg-hastingsite compositions return higher temperatures (~890–940 °C; Fig. 8). Plagioclase-melt and amphibole-melt equilibrium tests applied to the Singkut tuff reveal that only plagioclase crystals with An = 30–48 and amphibole crystals with Al^{IV} = 1–1.4 are in equilibrium with the matrix glass compositions (Fig. 7) and return narrower temperature intervals (~790–810 °C and ~ 780–840 °C, respectively). Magma water content in the Singkut tuff ranges between 4.5 and 4.8 wt% (Fig. 8). Mg-hornblende amphibole barometry indicate pressures between 0.7 and 2.3 kbar for the pre-caldera lavas, between 0.3 and 2.4 kbar for the Singkut tuff, and between 0.6 and 2.5 kbar for the post-caldera lavas. Median pressures vary from 1.1 to 1.5 kbar, corresponding to a 4–6 km depth range. Tschermakitic pargasite and Mg-hastingsite compositions record pressures between 3 and 3.9 kbar (Fig. 8). Amphibole oxy-barometry returns oxygen fugacities between NNO + 0.5 and NNO + 1.5 for all the studied units (Fig. 8).

Notably, Fe–Ti oxide thermometry and oxybarometry could not be applied to the pre-caldera and post-caldera lavas due to post-depositional modification to the original composition of the oxides. In the Singkut tuff, we observe no correlation between pre-eruptive
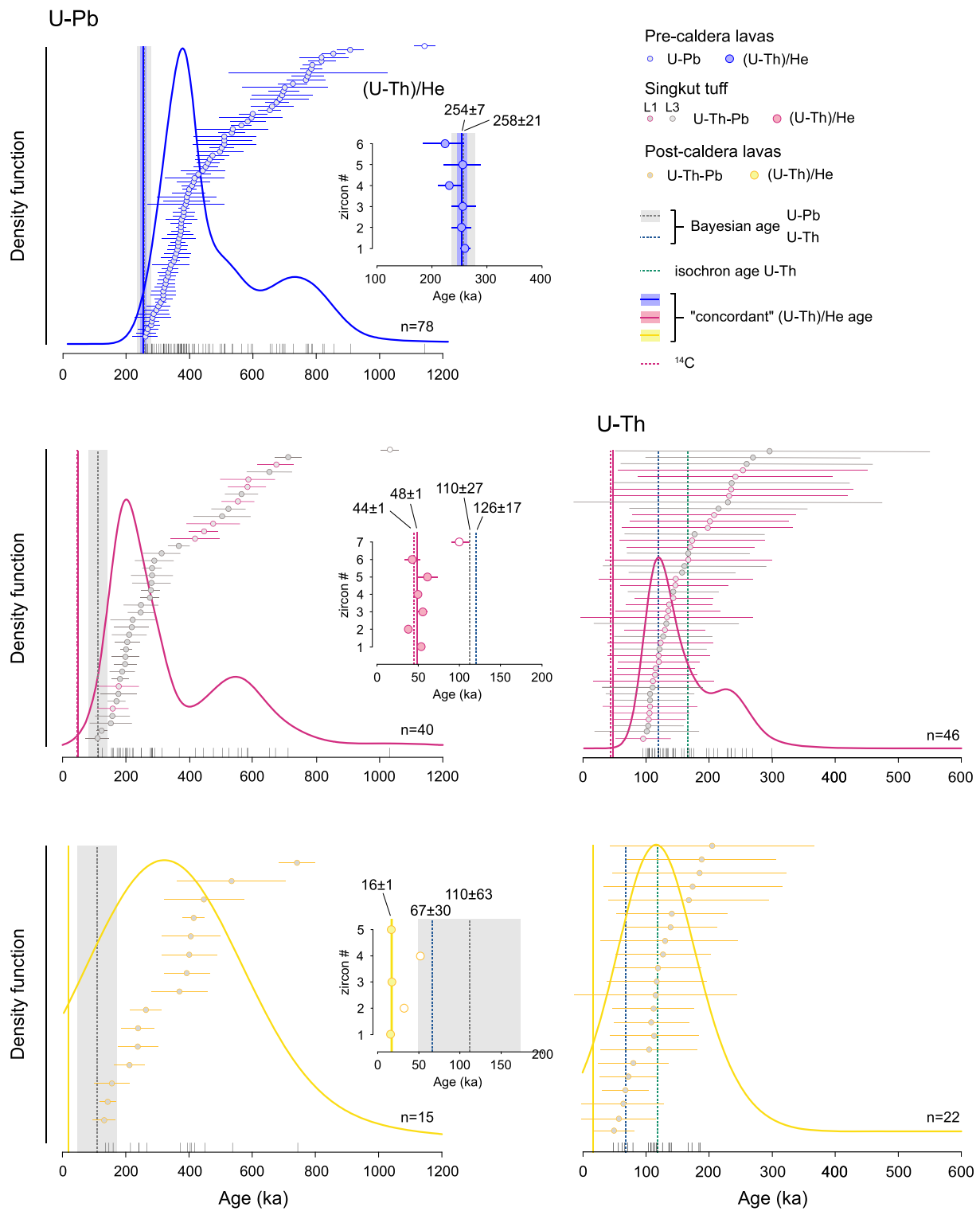
Fig. 9. Kernel density estimation (KDE) of the U–Pb (left panels) and U–Th (right panels) zircon crystallization ages (dots) with 2σ uncertainties. Empty symbols represent outliers. Small plots (center) show the disequilibrium-corrected (U–Th)/He zircon ages with 2σ uncertainties and (U–Th)/He "concordant" eruption ages and associated 2σ uncertainties obtained using the MCHeCalc computational routine (Schmitt et al., 2010). Empty symbols represent zircons excluded from eruption age calculations. Bayesian eruption age interpretations of the U–Pb and U–Th zircon crystallization ages were obtained using the model of Keller et al. (2018). U–Th single zircon ages are those obtained using the model of Boehnke et al. (2016). (^{238}U/^{232}Th) vs. (^{230}Th/^{232}Th) isochron ages as well as weighted mean radiocarbon age are reported for comparison.

temperatures obtained using Fe–Ti and Fe–Mg exchange between oxide pairs, with Fe–Mg temperatures being systematically higher (>250 °C) than Fe–Ti temperatures. Such behavior might reflect post-eruptive re-equilibration of the Fe–Ti oxide pairs (Ghiorso and Evans, 2008; Hou et al., 2020), thus we prefer not to use oxide compositions to estimate pre-eruptive parameters.

5.5. Geochronology

Zircon crystals from lavas and pyroclastics from Singkut describe wide age ranges, indicating protracted zircon crystallization in the Singkut magma reservoir (Fig. 9). Specifically, common Pb- and Th–U disequilibrium-corrected ^{238}U–^{206}Pb crystallization ages of single zircon crystals range between 908 ± 34 and 260 ± 40 ka (2σ) in the pre-caldera lavas, between 712 ± 43 and 112 ± 38 ka (2σ) in the Singkut tuff (L1 and L3) and between 742 ± 58 and 132 ± 36 ka (2σ) in the post-caldera lavas. In the pre-caldera lavas and Singkut tuff, two zircons with much older crystallization ages (1143 ± 34 and 1032 ± 36 ka, respectively) were recognized. In the Singkut tuff, U–^{230}Th single zircon crystallization ages span between secular equilibrium (>350 ka) and 99 ± 38 ka, when calculated using two point zircon-glass isochrons (Reid et al., 1997), or 93 ± 44 ka, using the model of Boehnke et al. (2016). In the post-caldera lavas, U–^{230}Th single zircon ages calculated with the two methods range between secular equilibrium and 67 ± 22 ka or 49 ± 33 ka, respectively. U–Th isochron ages of $166 + 24$–28 ka (2σ; MSWD = 1.3) and $118 + 22$–28 ka (2σ; MSWD = 1.6) were calculated for the Singkut tuff and post-caldera lavas, respectively. All U–Pb and U–Th data and plots are reported in the Supplementary Table 2.

In the pre-caldera lavas, the disequilibrium-corrected (U–Th)/He eruption ages of single zircon crystals from the pre-caldera lavas vary between ~220 and 260 ka and overlap within uncertainty (Fig. 9). The U–Pb crystallization ages of six zircons measured through depth profiles mostly range between ~475 and 250 ka showing some core-to-rim age variations. For these crystals, we used an average core-rim crystallization age (and associated uncertainty) to perform disequilibrium corrections of the Ftz-corrected He ages. Only one zircon displays a very strong core-to-rim age zoning (from ~60 Ma to 450 ka) with a clear prevalence of the older domain representing ~90% of the ablated volume (Supplementary Table 2). This indicates that the zircon was mostly in secular equilibrium at the time of the eruption. Hence, disequilibrium correction has no influence on the final (U–Th)/He age of this crystal. In the Singkut tuff, we performed (U–Th)/He dating of eight zircon crystals ranging in U–Pb and U–^{230}Th crystallization age between ~130 and 650 ka. Disequilibrium-corrected (U–Th)/He ages of seven crystals vary between ~38 and 59 ka, while one zircon shows a significantly older age

(~98 ka) (Fig. 9). Five zircons from the post-caldera lavas were double-dated. U–Pb crystallization ages of these zircons range between ~60 Ma and 180 ka, while disequilibrium-corrected (U–Th)/He ages vary between ~50 and 15 ka (Fig. 9).

Radiocarbon dating (^{14}C) of organic-rich material within the L2 subunit of the Singkut tuff produced a calibrated median age of $43,754 \pm 898$ cal a BP (2σ), while foraminifera sampled from the marine core GeoB10021–1 within the sediment interval directly above the volcanic ash layer correlated to the Singkut tuff, yielded a calibrated median age of $44,114 \pm 684$ cal a BP (2σ; Supplementary Table 2).

5.6. Eruption age calculations

We used the MCHeCalc computational routine (Schmitt et al., 2010) to calculate a best-fit eruption age for all the studied units by inputting the disequilibrium-corrected (U–Th)/He ages of single zircon crystals. The algorithm provides a "concordant" age distribution calculated from the intersection of all individual eruption ages with associated peak age, asymmetric uncertainties and a goodness-of-fit parameter (Q). We also compare the best-fit (U–Th)/He eruption ages with eruption age interpretations of the U–^{230}Th and ^{238}U–^{206}Pb zircon crystallization ages obtained using the Bayesian model of Keller et al. (2018). Results are reported in Fig. 9 and Supplementary Table 2.

For the pre-caldera lavas, a "concordant" eruption age of 254 ± 7 ka (2σ) was calculated based on the disequilibrium-corrected (U–Th)/He ages of all six zircons. This age overlaps within uncertainty with the Bayesian eruption age of 258 ± 21 ka (2σ) (Fig. 9), thus demonstrating that the emplacement of younger lava flows above the sampled lava flow did not result in resetting of the (U–Th)/He system in the analyzed zircons.

In the Singkut tuff, disequilibrium-corrected (U–Th)/He ages of seven crystals in pumices from L3 return a "concordant" eruption age of 48.0 ± 1.4 ka (2σ). One zircon showing an older He age (~98 ka) was excluded from best fit eruption age calculations. Two ^{14}C calibrated ages were obtained from organic-rich material found within L2 and foraminifera in the marine sediments above the Singkut tephra layer. The two ^{14}C calibrated ages perfectly overlap within uncertainty ($43,754 \pm 898$ and $44,114 \pm 684$ ya cal a BP, respectively), while the modeled (U–Th)/He zircon "concordant" eruption age is slightly older (Fig. 9). Given the consistency of the two independent radiocarbon calibrated ages, our preferred age for the Singkut caldera-forming eruption is $43,983 \pm 544$ (2σ), corresponding to the weighted mean of the two ^{14}C calibrated ages. Notably, both "concordant" (U–Th)/He and radiocarbon eruption ages are younger than the Bayesian eruption ages calculated using the U–Pb and U–^{230}Th crystallization ages (110 ± 27 and 126 ± 17 ka,

Table 1

Estimated minimum total volume of the Singkut tuff derived by adding: 1) the volume of pyroclastic density current (PDC) estimated using the area of the northern and southern sheets, inferred from the distribution of the deposits in the field (Fig. 2) and an average thickness of 25 m; 2) the volume of the intra-caldera inflow estimated based on the area delimited by the inferred caldera rim (Fig. 2) and the thickness of the intra-caldera tuff (500 m) as observed in several exploration wells located inside the Singkut caldera (Atmojo et al., 2000); and 3) the volume of the Plinian fallout and the fine ash component (co-ignimbrite ash) estimated using the method of Legros (2000) over a triangular area with a curved base, representing an ideal isopach shape. The main axis of this shape connects the vent (apex of the triangle) with the sampling location of the fallout out deposit (L1) and the marine core GeoB/10021/1 (prolongation of the main axis to encounter the semi-circle). We used two endmember apex angles (10° and 60°) to encompass a range of possible wind conditions affecting the width of the volcanic plume. The contribution of the fallout and fine ash components to the total erupted volume is minor (0.13 km³ for a 10° angle and 0.9 km³ for a 60° angle) and thus within the range of possible wind conditions the estimated minimum volume of the Singkut tuff ranges between 59 and 61 km³. Dense rock equivalent (DRE) volumes were calculated using the following ranges of porosity: intracaldera infill 33–45%; ignimbrite outflow 57–73%; fallout and co-ignimbrite ash 55–63% (Karstens et al., 2023). A density of 2.4 g/cm³ was used to calculate the mass. Values in parenthesis indicate averages.

Deposits	Area	Av. thickness	Isopach area (10–60°)	Thickness	Volume	DRE	Mass	Magnitude	VEI
	km²	km	km²	km	km³	km³	kg		
PDC outflow (N lobe)	1170	0.025			29.25	7.9–12.6			
PDC outflow (S lobe)	395	0.025			9.9	2.7–4.2			
Caldera infill	40	0.50			20	11–13.4			
Fallout (on-land)			10–508	8×10^5	0.003–0.15	0.002–0.09			
Distal ash (marine)			13,008–69,376	0.5×10^5	0.24–1.28	0.13–0.81			
Total					59–61 (60)	21.7–31.1 (26.4)	$5.2–7.5 \times 10^{13}$	6.7–6.9	6
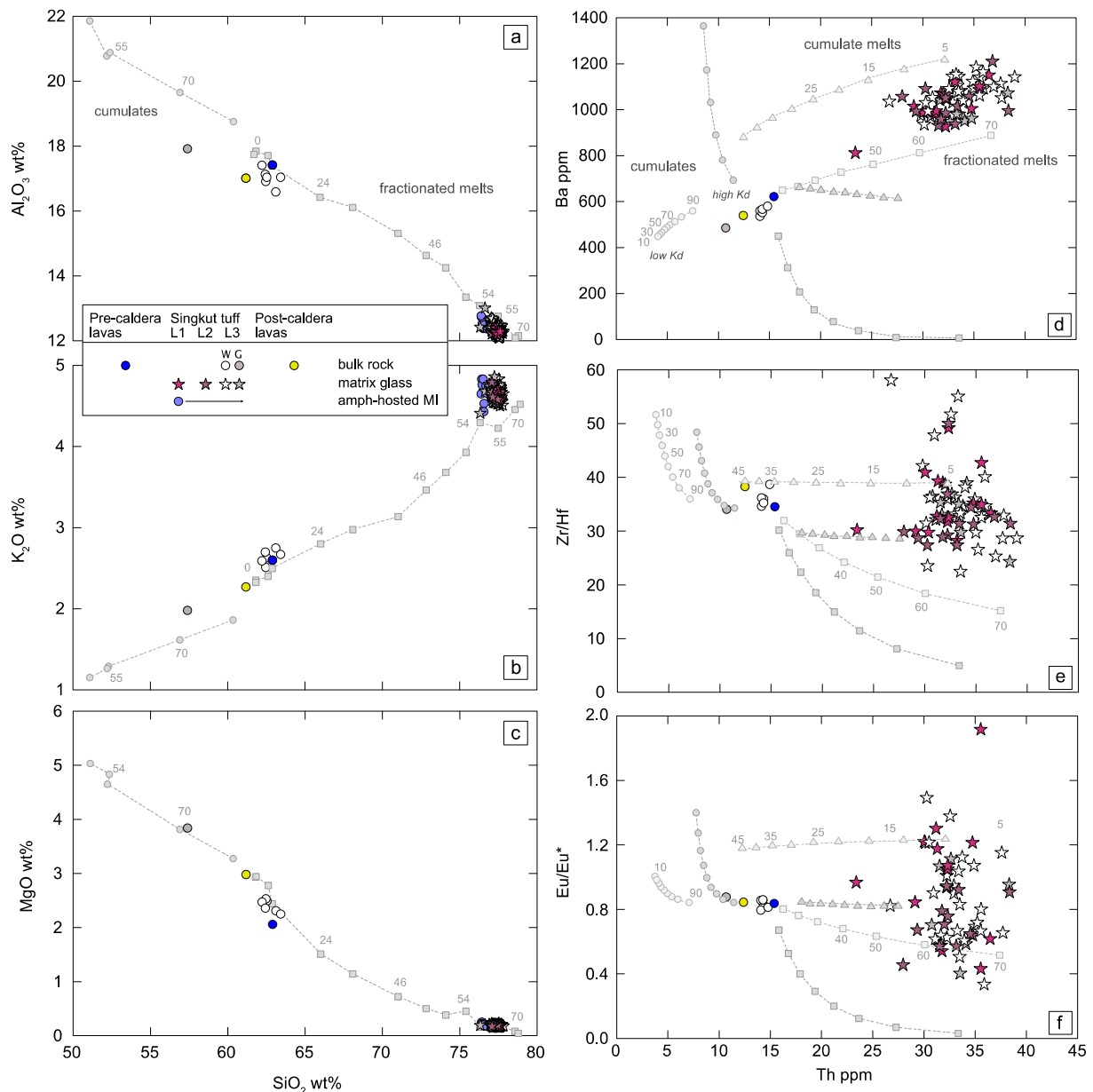
Fig. 10. Major element plots (a–c) showing Singkut bulk compositions compared to liquid lines of descent (gray dashed lines with squares) and cumulate lines of descent (gray dashed lines with dots) obtained using the experimental data of Marxer and Ulmer (2019). Gray symbols and numbers along the dashed lines indicate solid fractions. Trace element plots (d–f) showing the evolution of fractionated liquid (gray dashed lines with squares), cumulate (gray dashed lines with dots), and cumulate melt compositions (gray dashed lines with triangles). See Supplementary Table 4 for the details of the modeling. Gray squares, circles, and numbers along the dashed lines indicate the solid fractions produced via fractional crystallization, while gray triangles and numbers indicate the melt fraction produced by cumulate melting. Light gray colors refer to results obtained using low Kds, while darker gray colors refer to results obtained using high Kds. W = white pumices; G = gray pumices.

respectively; Fig. 9).

(U–Th)/He ages of single zircons from the post-caldera lavas define a wide range. He measurements of these zircons were particularly challenging due to their young age and small crystal size resulting in high helium blank/sample ratios and large alpha-ejection corrections (Supplementary Table 2). We calculated a tentative eruption age using 3 zircons that define a clear age cluster and obtained a "concordant" eruption age of 16.3 ± 0.6 ka (2σ). Two zircons showing older ages (~50 and 32 ka) were excluded from the eruption age calculation (Fig. 9). Similar to what we observed in the Singkut tuff, the (U–Th)/He "concordant" eruption age is younger than the Bayesian eruption ages calculated using the U–Pb and U–^{230}Th crystallization ages (110 ± 63 and 67 ± 30 ka, respectively; Fig. 9).

Crystals with older (U–Th)/He age are often interpreted as xenocrysts entrained during eruption but not completely reset (e.g., Schmitt et al., 2010). This could be a possibility for the zircons from the post-caldera lavas, whose age is comparable to that of the Singkut tuff. Indeed, post-caldera magmas likely travelled through the thick intra-caldera Singkut tuff deposits before being erupted. However, we consider unlikely that xenocrystic material could be incorporated in the Singkut tuff without being reheated above the He closure temperature (~180 °C). Moreover, the Singkut tuff zircon with an older (U–Th)/He age (z9; Supplementary Table 2) has a crystallization age compatible with the main age peak distinguished in zircons from this unit (~200 ka; Fig. 9). Hence, we suggest that the older (U–Th)/He age might be the result of "He implantation" from other U-Th-rich neighbouring mineral

phases or due to the presence of fluid inclusions with excess He that we could not detect under the microscope (Flowers et al., 2022) or simply to the effect of ananlytical uncertainties that we cannot account for, possibly related to the large helium-blank and alpha-ejection corrections.

6. Discussion

6.1. Eruptive history of the Singkut caldera

Singkut preserves a rich stratigraphic record of its volcanic activity from the pre- to the post-caldera stages. Evidence of the pre-caldera effusive phases can be observed in the southern and southwestern sectors of the caldera where crystal-rich and quartz-bearing dacitic lavas crop out. These lavas represent the remnants of a pre-caldera volcanic edifice, with activity dating back to at least ~254 ka (Fig. 9).

The present caldera structure formed as a consequence of a large explosive eruption that produced a monotonous, crystal-rich, andesitic to dacitic ignimbrite (i.e., Singkut tuff). The three distinct subunits (L1-L3; Fig. 2) recognized within the Singkut tuff pyroclastic sequence were deposited during different phases of the eruption: layer L1 is a fallout deposit, emplaced during an initial Plinian phase, whereas L2 and the base of L3 were likely deposited by ash-rich pyroclastic density currents (PDCs) that formed when the Plinian column started to collapse. During the climactic phase of the eruption, an increase of the mass discharge rate resulted in the deposition of massive pumice-rich PDC deposits, representing the bulk of L3, and eventually culminated in caldera collapse. Both the occurrence of organic material within the L2 and the presence of an erosive contact separating L1 from L2 support the hypothesis that L2 was deposited during the initial phases of collapse of the Plinian column. The increasing abundance of crystal-rich gray pumices (up to 62 vol% crystals) towards the top of L3 (Fig. 4) indicates that during its final stages the eruption was tapping the bottom of the magma reservoir where the most crystalline material was stored. The presence of a distal tephra layer in the marine core GeoB10021–1 (Figs. 1 and S1) suggests that volcanic ash was transported for >300 km to the southwest of the source either during the Plinian phase or from a co-ignimbrite cloud under the influence of prevailing wind conditions dominated by

the seasonal northeastern and southwestern monsoons (Dash, 2005; Lo and Orton, 2016). Given the modest thickness of the fallout deposits ~14 km from the source (~8 cm), we consider unlikely that a considerable amount of Plinian fallout material could be transported to the distal core location producing a ~0.5 cm-thick ash layer. Thus, our preferred interpretation is that the marine tephra layer represents a co-ignimbrite ash deposit. Based on this interpretation, we used the method of Legros (2000) to calculate the minimum volume of the onshore Plinian fallout and the offshore co-ignimbrite deposit employing single isopachs. The volume of the outflow PDC deposits was calculated based on the area of the northern and southern ignimbrite sheets and an average thickness of 25 m, while for the intracaldera deposits we used the area delimited by the caldera rims and an intracaldera tuff thickness of 500 m, as reported in exploration studies of Atmojo et al. (2000). More details on erupted volume calculations are reported in Table 1.

We estimate that the Singkut caldera-forming eruption discharged a minimum bulk tephra volume of ~60 km³, corresponding to ~26 km³ of DRE, and thus should be classified as a VEI 6 eruption.

After the caldera-forming eruption, magmatic activity resumed at the rims and inside the caldera, forming three volcanic centers. Such activity was mostly effusive whereas the most recent manifestations at Mt. Sibayak were explosive, indicating a possible change in eruptive style with time. We sampled an andesitic lava from a volcanic center located inside the caldera (i.e., Mt. Pratektekan) and obtained a tentative "concordant" eruption age of ~16 ka using disequilibrium corrected (U–Th)/He ages of three zircons.

6.2. Geochemical variability of Singkut magmas

Singkut pumices and lavas vary in bulk-rock composition from andesites to dacites with rhyolitic matrix glass and melt inclusions (Fig. 5). Geochemical trends of major elements in the Singkut magmas closely resemble those obtained with fractional crystallization experiments of arc magmas at 0.2 GPa and in oxidized conditions (NNO oxygen buffer) using a tonalite starting composition (Marxer and Ulmer, 2019). Experimental conditions are similar to those obtained for the Singkut magmas (Fig. 8), the mineral assemblage in the experiments matches that of Singkut and the starting compositions are similar to those of bulk-
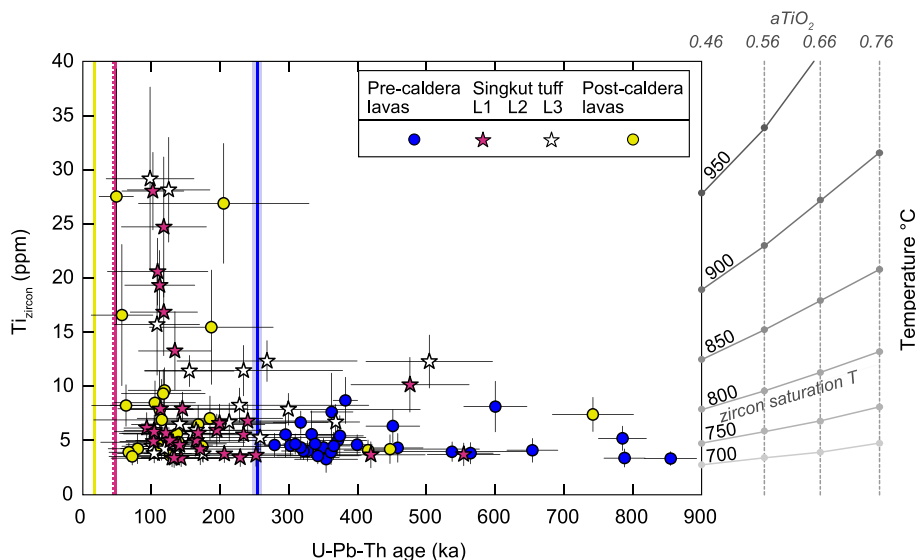
Fig. 11. Zircon Ti content and Ti-in-zircon temperatures vs. U-Th-Pb zircon crystallization ages. Ti content is corrected to zircon reference material compositions of Szymanowski et al. (2018). Ti-in-zircon temperatures were calculated with the calibration of Ferry and Watson (2007). An aTiO$_2$ of 0.46 was calculated using Rhyolite-MELTS and aSiO$_2$ inferred based on the presence of quartz (=1). The plot on the right shows how the Ti-in-zircon temperature scale changes with aTiO$_2$ within a range of 0.46–0.76 (values typically used for SiO$_2$-rich magmas). Gray lines are isotherms while gray dots indicate the position of each temperature value at different aTiO$_2$ (vertical dashed lines). Overall, higher values of aTiO$_2$ result in lower Ti-in-zircon temperatures. Zircon saturation temperatures are calculated with the model of Crisp and Berry (2022) using the matrix glass with low Zr/Hf.

rock white pumices and lavas, while gray pumices are significantly more mafic (i.e., enriched in FeO, MgO, Al_2O_3, CaO, TiO_2) and closely resemble cumulate compositions (Figs. 10 and S3). Experimentally derived liquid lines of descent show that rhyolitic compositions, akin to those of Singkut glasses, can be reached at around 55 to 70% solid fraction (Figs. 10 and S3). Magma evolution involves early crystallization of plagioclase, clinopyroxene and orthopyroxene, followed by amphibole, Fe–Ti oxides, biotite, and quartz. Plagioclase and amphibole largely dominate the crystal assemblage. The lack of clinopyroxene in the Singkut mineral assemblage is coherent with the disappearance of this phase during peritectic reaction between clinopyroxene and residual liquid to form amphibole (Marxer and Ulmer, 2019). In the experiments, crystallization of amphibole at the expense of clinopyroxene occurs at around 900 °C, in line with temperatures obtained for the Singkut magmas via amphibole thermometry (Fig. 8).

Crystallization of plagioclase, orthopyroxene, and amphibole leads to a decrease of FeO, MgO, CaO, and Al_2O_3 and an increase of K_2O in the residual melt, while TiO_2 drop marks the onset of oxide crystallization (Figs. 10 and S3). Biotite and quartz join the mineral assemblage at around 750 °C and 55% melt fraction (Marxer and Ulmer, 2019). Coherently, trace element modeling using the pre-caldera lava as starting composition and a range of bulk-rock partition coefficients (Supplementary Table 4), shows that rhyolitic compositions can be reached after ~50–70% fractional crystallization (Fig. 10). Derived cumulate mineral assemblages are mainly composed of plagioclase and amphibole together with lesser amounts of biotite, quartz, pyroxene, Fe–Ti oxides, and accessory zircon and apatite. This mineral assemblage mirrors that observed in the Singkut rocks (Fig. 3). Fractionation of these phases drives the residual liquids to lower Sr, Eu/Eu*, Zr/Hf, MREE, and HREE contents and higher Ba and Th contents. However, fractional crystallization alone does not explain the positive Eu anomalies and supra-chondritic Zr/Hf ratio observed in the matrix glass compositions (Figs. 6 and 10).

6.3. Evidence of cumulate melting

Major and trace element patterns show that fractional crystallization processes played a primary role in the evolution of the Singkut magmas. Such processes generated silicic cumulates dominated by plagioclase and amphibole, enriched in Al_2O_3, MgO, CaO, FeO, TiO_2, Sr, MREE, and HREE and depleted in K_2O, Th, and Ba compared to their residual rhyolitic melts. Additionally, accumulation of plagioclase and zircon produced cumulate compositions with positive Eu anomalies and supra-chondritic Zr/Hf ratios (Figs. 6 and 10).

When crystallizing magmas reach a solid fraction of 50–70%, they approach the rheological lockup threshold (Huber et al., 2011) and need an external source of heat and volatiles to develop into eruptible magma bodies. Such a source, typically provided by more mafic, hotter, and volatile-rich recharge, can trigger partial melting of the cumulate mush and lower its crystallinity below the rheological lockup (Ellis et al., 2023). At Singkut, we find textural evidence of re-heating in the form of resorbed quartz crystals in the pre-caldera lavas (Fig. 3). Quartz is scarce in the Singkut tuff and is only present in traces in the post-caldera lavas indicating progressive consumption of quartz over time. Plagioclase represents the most abundant mineral phase in the Singkut rocks, but crystals in equilibrium with the melt are extremely scarce (Fig. 7). Such evidence, together with the positive Eu anomalies detected in some of the matrix glass compositions, suggest melting of low An plagioclase crystals in the cumulate mush. High Ba contents in matrix glasses might be ascribed to biotite breakdown, while super-chondritic Zr/Hf ratios likely derive from zircon melting (Deering and Bachmann, 2010; Ellis et al., 2023). Trace element modeling shows that partial melting of a cumulate formed after 70% fractional crystallization, akin to the gray pumice bulk composition, produces liquids with higher Eu/Eu*, Zr/Hf,

and Ba compared to their fractionated melts, while mixing between different proportions of cumulate melts, cumulate material and fractionated melts can generate the bulk-rock composition of white pumices and lavas (Fig. 10).

6.4. Mechanisms and timescales of cumulate mush remobilization

Using a combination of textural observations and geochemical data we have shown that cumulate melting played a key role in allowing remobilization and eruption of a large crystal mush stored at shallow depth below Singkut. Additionally, Ti-in-zircon temperatures, U–Pb and U–^{230}Th zircon crystallization ages, and their comparison with (U–Th)/He and ^{14}C eruption ages provide important information about the nature and timescales of these processes. Ti-in-zircon temperatures were calculated using the calibration of Ferry and Watson (2007). The activity of TiO_2 (aTiO_2 = 0.46) was estimated via Rhyolite-MELTS (Gualda et al., 2012) using the bulk-rock composition of pre-caldera lavas as starting composition with 4 wt% water content, a pressure of 150 MPa and oxygen fugacity fixed at the NNO oxygen buffer. In Fig. 11, we show how temperatures change within a range of aTiO_2 commonly used in the literature for Ti-in-zircon thermometry (e.g., Reid et al., 2011; Szymanowski et al., 2017). The activity of SiO_2 was set at 1 due to the presence of quartz crystals in the pre-caldera lavas and traces of quartz in the other units. We note that a decrease of the aSiO_2 in magma due to quartz melting (e.g., from 1 to 0.9) would lead to a negligible decrease of Ti-in-zircon temperatures (~ 10 °C) and thus would not affect our interpretation.

In the pre-caldera lavas, zircon crystallization occurred continuously for at least ~650 ky before eruption and the Bayesian eruption age obtained using the U–Pb zircon age distribution overlaps within uncertainty with the (U–Th)/He "concordant" eruption age (Fig. 9), indicating that magmas remained zircon saturated until eruption. Ti-in-zircon thermometry confirms that during this time the temperature within the magma reservoir was relatively stable and close or below zircon saturation (Fig. 11). In the Singkut tuff and post-caldera lavas, the Bayesian eruption age calculated using U–Pb and U–^{230}Th zircon crystallization ages are older than eruption ages obtained either by (U–Th)/He or radiocarbon dating (Fig. 9), and zircon crystals commonly appear resorbed and are less abundant compared to the pre-caldera lavas (Fig. S6).

A temperature increase (from ~850 to 950 °C, for aTiO_2 = 0.46) is recorded in zircons from these two units starting approximately from 250 ka and until the caldera-forming eruption (~44 ka), which marks the last recorded episode of zircon crystallization (Fig. 11). Heating likely triggered the breakdown of quartz, plagioclase, zircon (and potentially biotite) in the cumulate mush and generated a cumulate melt with the geochemical signature observed in the matrix glass (Fig. 10). We hypothesise that these thermal conditions initially affected portions of the highly crystalline reservoir, as indicated by the co-existence of high and low temperature zircons in the Singkut tuff and post-caldera lavas (Fig. 11), and eventually drove the system out of zircon saturation, both erasing the youngest zircon growth domains and hampering new zircon crystallization. Such behavior is expected in calcalkaline systems with relatively low Zr cumulate melts (Szymanowski et al., 2020), closely resembling our modeled cumulate compositions (Supplementary Table 4). We cannot exclude that the age gap between the youngest zircon population in our data and the eruption age of the Singkut tuff and post-caldera lavas is due to under-sampling during in-situ analyses. However, we have presented several textural and geochemical lines of evidence indicating that the Singkut magma body experienced heating and that zircon melting likely occurred, leaving a clear trace in the glass geochemistry (Fig. 10e). Moreover, in contrast with the pre-caldera lavas, near-eruption ages were not even detected in the shallowest measured material within depth profiles of zircons from
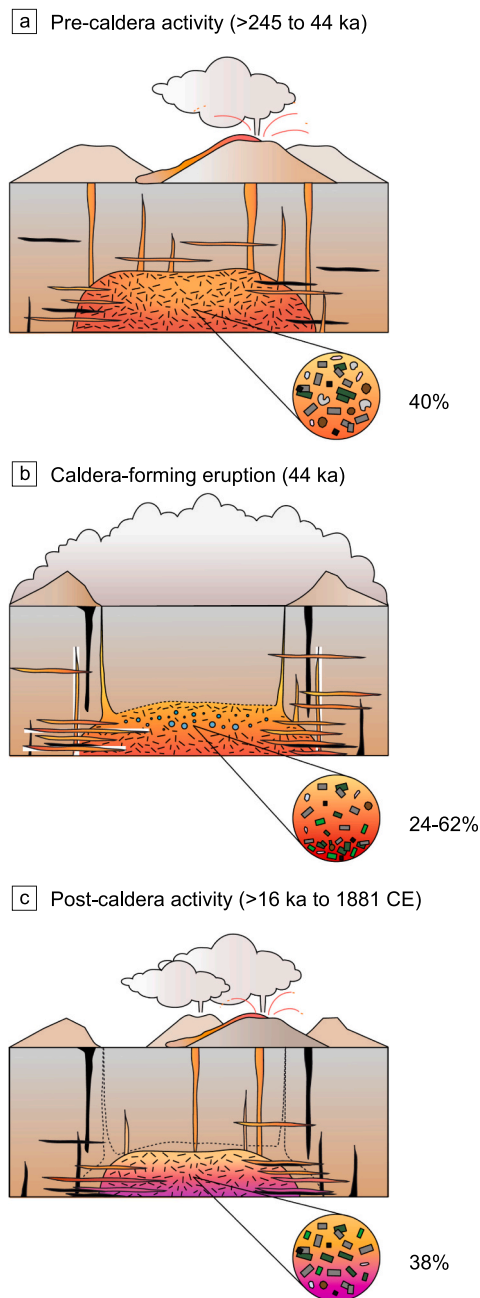
Fig. 12. Cartoon showing the different evolutionary phases of the Singkut caldera: a) prolonged mostly effusive activity forming pre-caldera volcanoes (>254–44 ka); b) catastrophic explosive eruption producing the Singkut tuff and consequent caldera-collapse (44 ka) and c) post-caldera recovery leading to the generation of volcanic centres close to the rims and inside the Singkut caldera (>16 ka – 1881 CE). Insets display the mineralogy and crystallinity of magmas erupted during the three phases: quartz (light gray), plagioclase (darker gray), amphibole (dark green), orthopyroxene (light green), biotite (brown), Fe–Ti oxides (black), zircon (pink), apatite (light blue). Percentages refer to the vol% crystals. In the Singkut tuff the crystallinity varies between 24 and 42 vol% crystals in the white pumices and between 42 and 62 vol% crystals in the gray pumices. Note that: 1) resorbed quartz is only present in the pre-caldera lavas while it is missing in the Singkut tuff and post-caldera lavas; 2) zircons are more abundant and more euhedral in the pre-caldera lavas compared to the Singkut tuff and post-caldera lavas; 3) orthopyroxene is more abundant in the Singkut tuff and post-caldera lavas compared to the pre-caldera lavas and 4) recharge (red-purple gradients in magma reservoir) increases from a) to c). See text for more explanations. (For interpretation of the references to color in this figure legend, the reader is referred to the web version of this article.)

the Singkut tuff and the post-caldera lavas (Supplementary Table 2). For these reasons we consider the under-sampling interpretation unlikely.

The cause of a progressive temperature increase could be related to an increase of the recharge flux below the Singkut upper crustal reservoir starting at the time of the eruption of pre-caldera lavas, as indicated by the textural evidence of quartz melting (Fig. 3a,b) and the appearance of zircons with higher Ti (Fig. 11). Indeed, it has been shown that during the growing phases that precede large eruptions, upper crustal reservoirs tend to attract magma supply from deeper crustal levels by focusing the surrounding dikes (Karlstrom et al., 2009; Pansino and Taisne, 2019). Notably, at Singkut the highest Ti-in-zircon temperatures (~900–950 °C) are comparable to those of the deeper and hotter Tschermakite-pargasitic and Mg-hastingsitic amphiboles that were likely brought into the reservoir by recharge (Fig. 8) and the presence of these amphiboles, together with orthopyroxene with higher Mg#, only in the Singkut tuff and post-caldera lavas might indicate that recharge was volumetrically more important during this time.

Recharge not only caused a temperature increase but likely brought more volatiles into the shallow reservoir, facilitating cumulate melting and consequently crystal mush unlocking by self-assimilation (Huber et al., 2011). Volatile addition might have allowed the reservoir to reach saturation before the Singkut caldera-forming eruption, a condition that typically promotes reservoir growth during the pre-caldera phases (Huber et al., 2019). Indeed, the water content estimated using plagioclase-melt hygrometry (4.5–4.8 wt%) is very close to or above water saturation in rhyolitic magmas at storage conditions similar to those inferred for the Singkut tuff (4.5 wt% at 150 MPa and 800 °C; Liu et al., 2005). Additionally, the presence of low analytical total biotites only in the Singkut tuff could be the result of crystallization in volatile saturated conditions, leading to the entrapment of a volatile phase in the crystal structure as interlayer fluid inclusions (Ellis et al., 2022). Alternatively, low analytical total could be the result of interaction with meteoric-hydrothermal fluids immediately after eruption. The different trends identified in the K_2O vs. CaO plot (Fig. S5) could be ascribed to variable degrees of interaction between the fluids and the deposit in the different portions of the ignimbrite as proposed by Wolff and Neukampf (2022) for the Battleship Rock Ignimbrite (Valles Caldera, USA). More mineralogical and geochemical investigations would be needed to provide a definitive interpretation.

6.5. Phenocryst content controls on eruption styles at Singkut

Important differences in crystallinity are observed between the lavas (40–50 vol% crystals) and the pumices (24–62 vol% crystals), and a clear trend of increasing crystallinity from bottom to top is observed in the ignimbrite sequence (Fig. 4). Crystallinity is known to have a non-linear positive influence on magma viscosities with little impact between 0 and ~ 30 vol% crystals and a major impact between 30 and 60 vol% crystals, until the magma becomes rheologically locked (>60–80 vol% crystals; Huber et al., 2011). Applying the model of Giordano et al. (2008) to estimate melt viscosities in the Singkut tuff at 800 °C and with 4.5 wt% water, we obtain ~10^5 Pa·s. Addition of 40% crystals produces magma viscosities >10^6 Pa·s. This value represents a critical viscosity limit above which magmas need extreme strain rates to be mobilized and thus would fall with most models in an effusive regime (Gonnermann and Manga, 2013; Popa et al., 2021). The high crystallinity of the lavas, their modest volumes suggesting modest magma discharge rates and the presence of amphibole breakdown rims (Fig. 3 a,b) implying low magma decompression rates (Rutherford and Hill, 1993) are strong arguments to explain the effusive eruption style. Phenocrysts control explosivity by increasing the overall magma viscosity, which in turn leads to low magma decompression rate and enhances bubble coalescence by mechanical effect (Kushnir et al., 2017; Lindoo et al., 2017) promoting outgassing efficiency (Castro and Gardner, 2008; Colombier et al., 2017; Bernard and Bouvet de Maisonneuve, 2020).

In the Singkut tuff, the relatively low crystal content of magmas

discharged at the beginning of the eruption (L1 and L2), derived by recharge-induced partial melting of the cumulate crystal mush, might have played an important role in shifting the eruption style to an explosive regime. Indeed, a lower crystallinity (and lower viscosity) allowed magma to move faster in the conduit (as testified to the absence of amphibole breakdown rims in the Singkut tuff; Fig. 3c,d) hampering volatile loss upon magma ascent. Towards the latest phases of the eruption, when the most crystalline portions were erupted, fast ascent resulted in an increase in shearing in the conduit as testified by the presence of shattered crystals in the Singkut tuff (Fig. 3c,d). Such mechanism has been shown to be particularly efficient in intermediate to crystal-rich magmas (>40 vol%) and to promote apparent shear-thinning behavior of the melt with crystal re-organisation along flow bands (Cordonnier et al., 2012, 2009; Kolzenburg et al., 2022), allowing even the higher crystallinity magmas to keep erupting explosively. We suggest that the removal of the lower crystallinity magma at the beginning of the climactic eruption might have initiated a runaway effect that led to the emptying of the magma reservoir and the caldera collapse. The increasing occurrence of gray pumices, which we interpret as portions of the cumulate crystal mush, towards the top of the pyroclastic sequence implies that the eruption may have stopped by 'self-choking' when only the most crystalline portion of the reservoir remained to be erupted.

The post-caldera lavas display slightly lower crystallinities and a more mafic signature compared to the pre-caldera lavas. These characteristics, together with a relatively large gap between the Bayesian estimate from zircon crystallization ages and the (U/Th)/He eruption age (~50 ky), indicate that mafic recharge bringing heat, mass and volatiles into the reservoir was important after the caldera-forming eruption when the magmatic system had experienced major decompression and devolatilization. We hypothesise that the post-caldera lavas represent a phase of slow rebuilding of the reservoir and slow build-up of the overpressure allowing small quantities of crystal-rich magmas to find ways to the surface through the pathways opened during caldera collapse. A mild overpressure coupled with a high crystallinity resulted in effusive eruption. This eruptive style has been commonly observed during the post-collapse phases of activity at many silicic caldera-forming systems (e.g., Yellowstone, USA, Girard and Stix, 2012, Till et al., 2019; Valles, USA, Wolff and Gardner, 1995; Kennedy et al., 2012; Santorini, Greece, Druitt et al., 1999; Fabbro et al., 2017; Toba, Indonesia, de Silva et al., 2015; Mucek et al., 2017; Altiplano-Puna, Central Andes; Tierney et al., 2016).

7. Conclusions

Using a combination of field observations, textural, geochemical, and geochronological data we have provided the first volcanological and petrological characterization of the Singkut caldera (northern Sumatra, Indonesia). Magmatic activity at Singkut started effusively at least at ~254 ka and culminated at ~44 ka in a large caldera-forming eruption (~26 km^3 DRE; VEI 6; Fig. 12) that spread volcanic ashes hundreds of km away from the source. Effusive to mildly explosive post-caldera activity continued until historical time forming three volcanic cones (Fig. 12). During its lifetime, Singkut produced silicic magmas with similar composition and mineralogy, stored in a shallow crustal reservoir (~5 km) in a high crystallinity state, close to the rheological lock-up. We have shown that cumulate melting played a fundamental role in determining the eruptibility of these magmas and controlled the transition of eruptive style between the predominantly effusive pre- and post-caldera phases of activity and the explosive caldera-forming eruption. Our geochronological data suggest that thermal rejuvenation of the Singkut magma body started ~200 ky before the caldera-forming eruption and continued during the post-caldera activity due to increasing recharge with magmas of deeper origin into the shallow reservoir (Fig. 12). Such timescales are relatively long compared to those estimated using zircon petrochronology at other volcanoes (e.g.,

10s to 1000s years for small silicic eruptions at the Lassen Volcanic Center; Klemetti and Clynne, 2014) but similar to those obtained for other crystal-rich systems producing large eruptions (e.g., ~200 kyr for the Fish Canyon tuff, Wotzlaw et al., 2013, and ~50 ky for the Kneeling Nun tuff, Szymanowski et al., 2019). Previous studies (Huber et al., 2012; Cooper and Wilson, 2014; Audétat et al., 2023) have suggested that mush reactivation timescales might depend upon the size and thermal status of the reservoir and thus they tend to be longer in large, crystal-rich reservoirs compared to small and/or dominantly crystal-poor magma bodies. Much storter mush rejuvenation timescales (on the order of 10s to 1000s of years) have been estimated for large crystal-rich magma bodies using Ti-in-quartz diffusion modeling (e.g., Matthews et al., 2012; Tavazzani et al., 2020; Zhao et al., 2023). However, in shallow crustal silicic reservoirs, quartz crystallizes at lower temperature and higher solid fraction compared to zircon (Marxer and Ulmer, 2019). Hence, Ti-in-quartz diffusion modeling records the timing of quartz resorption and rim growth associated with the latest stages of mush rejuvenation, while zircon may capture a more extended time frame of magma reservoir evolution. Furthermore, Ti-in-quartz diffusion chronology is affected by significant uncertainites connected with the experimentally derived diffusion parameters (Audétat et al., 2023).

Further petrological investigations of the recently erupted magmas at Singkut would be necessary to determine the current status and future behavior of the magmatic system. Particularly, a progressive increase of the mafic signature of erupted products following the trend observed in our sample from the post-caldera lavas could suggest that the upper crustal reservoir is going through a recovery phase, potentially leading to the start of a new caldera cycle. Such behavior has been recognized in the post-caldera phases of activity at many other silicic calderas around the world (e.g., Campi Flegrei, Italy; Rabaul, Papua New Guinea; Okataina, New Zealand; Bouvet de Maisonneuve et al., 2021).

CRediT author statement

Francesca Forni: Conceptualization, Investigation, Visualization, Writing – Original Draft, Writing – Review and Editing. **Marcus Phua:** Investigation, Writing – Original Draft, Writing – Review and Editing. **Olivier Bernard:** Conceptualization, Investigation, Visualization, Writing – Original Draft, Writing – Review and Editing. **Maria Giuditta Fellin:** Investigation, *Validation,* Writing – Review and Editing. **Jeffrey Oalmann:** Investigation, Methodology, *Validation,* Writing – Review and Editing. **Colin Maden**: Resources, Writing – Review and Editing. **Hamdi Rifai:** Resources. **Caroline Bouvet de Maisonneuve:** Conceptualization, Funding Acquisition, Writing – Review and Editing.

Declaration of Competing Interest

The authors declare that they have no known competing financial interests or personal relationships that could have appeared to influence the work reported in this paper.

Data availability

All data provided in the supplementary tables

Acknowledgements

this paper.

Appendix A. Supplementary data

Supplementary data to this article can be found online at https://doi.org/10.1016/j.jvolgeores.2023.107971.

References

Atmojo, J.P., Itoi, R., Tanaka, T., Fukuda, M., Sudarman, S., Widiyarso, A., 2000. Modeling studies of Sibayak geothermal reservoir, Northern Sumatra, Indonesia. In: Presented at the Proceedings of the World Geothermal Congress, pp. 2037–2043.

Audétat, A., Schmitt, A.K., Njul, R., Saalfeld, M., Borisova, A., Lu, Y., 2023. New constraints on Ti diffusion in quartz and the priming of silicic volcanic eruptions. Nat. Commun. 14, 4277.

Bachmann, O., Bergantz, G.W., 2004. On the origin of crystal-poor rhyolites: Extracted from batholithic crystal mushes. J. Petrol. 45, 1565–1582. https://doi.org/10.1093/Petrology/Egh019.

Bachmann, O., Huber, C., 2016. Silicic magma reservoirs in the Earth's crust. Am. Mineral. 101, 2377–2404. https://doi.org/10.2138/am-2016-5675.

Bachmann, O., Dungan, M.A., Bussy, F., 2005. Insights into shallow magmatic processes in large silicic magma bodies: the trace element record in the Fish Canyon magma body, Colorado. Contrib. Mineral. Petr. 149, 338–349. https://doi.org/10.1007/S00410-005-0653-Z.

Bacon, C.R., Druitt, T.H., 1988. Compositional evolution of the zoned calcalkaline magma chamber of Mount Mazama, Crater Lake, Oregon. Contrib. Mineral. Petrol. 98, 224–256. https://doi.org/10.1007/BF00402114.

Bacon, C.R., Hirschmann, M.M., 1988. Mg/Mn partitioning as a test for equilibrium between coexisting Fe-Ti oxides. Am. Mineral. 73, 57–61.

Bernard, O., Bouvet de Maisonneuve, C., 2020. Controls on eruption style at Rabaul, Papua New Guinea–insights from microlites, porosity and permeability measurements. J. Volcanol. Geotherm. Res. 406, 107068.

Bernard, O., Bouvet de Maisonneuve, C., Arbaret, L., Nagashima, K., Oalmann, J., Prabowo, A., Ratdomopurbo, A., 2022. Varying processes, similar results: how composition influences fragmentation and subsequent feeding of large pyroclastic density currents. Front. Earth Sci. 10.

Boehnke, P., Barboni, M., Bell, E.A., 2016. Zircon U/Th model ages in the presence of melt heterogeneity. Quat. Geochronol. 34, 69–74. https://doi.org/10.1016/j.quageo.2016.03.005.

Bohrson, W.A., Reid, M.R., 1997. Genesis of silicic peralkaline volcanic rocks in an ocean island setting by crustal melting and open-system processes: Socorro Island, Mexico. J. Petrol. 38, 1137–1166. https://doi.org/10.1093/Petrology/38.9.1137.

Bouvet de Maisonneuve, C., Bergal-Kuvikas, O., 2020. Timing, magnitude and geochemistry of major Southeast Asian volcanic eruptions: identifying tephrochronologic markers. J. Quat. Sci. 35, 272–287. https://doi.org/10.1002/jqs.3181.

Bouvet de Maisonneuve, C., Forni, F., Bachmann, O., 2021. Magma reservoir evolution during the build up to and recovery from caldera-forming eruptions – a generalizable model? Earth Sci. Rev. 218, 103684 https://doi.org/10.1016/j.earscirev.2021.103684.

Burgisser, A., Bergantz, G.W., 2011. A rapid mechanism to remobilize and homogenize highly crystalline magma bodies. Nature 471, 212–215. https://doi.org/10.1038/nature09799.

Cameron, N.R., Aspden, J.A., Bridge, D.M., Djunuddin, A., Ghazali, S.A., Harahap, H., Hariwidjaja, Johari, S., Karawa, W., Keats, W., Ngabito, H., Rock, N.M.S., Whandoyo, R., 1982. Geologic Map of the Medan Quadrangle, Sumatra.

Castro, J.M., Gardner, J.E., 2008. Did magma ascent rate control the explosive-effusive transition at the Inyo volcanic chain, California? Geology 36, 279–282.

Chesner, C.A., 1998. Petrogenesis of the Toba Tuffs, Sumatra, Indonesia. J. Petrol. 39, 397–438. https://doi.org/10.1093/petroj/39.3.397.

Chesner, C.A., Rose, W.I., 1991. Stratigraphy of the Toba Tuffs and the evolution of the Toba Caldera Complex, Sumatra, Indonesia. Bull. Volcanol. 53, 343–356. https://doi.org/10.1007/BF00280226.

Chesner, C.A., Rose, W.I., Deino, A., Drake, R., Westgate, J.A., 1991. Eruptive history of Earth's largest Quaternary caldera (Toba, Indonesia) clarified. Geology 19, 200–203. https://doi.org/10.1130/0091-7613(1991)019<0200:Ehoesl>2.3.Co;2.

Colombier, M., Gurioli, L., Druitt, T., Shea, T., Boivin, P., Miallier, D., Cluzel, N., 2017. Textural evolution of magma during the 9.4-ka trachytic explosive eruption at Kilian Volcano, Chaîne des Puys, France. Bull. Volcanol. 79, 1–24.

Cooper, K.M., 2017. What does a magma reservoir look like? The "crystal's-eye" view. Elements 13, 23–28. https://doi.org/10.2113/gselements.13.1.23.

Cooper, K.M., Kent, A.J.R., 2014. Rapid remobilization of magmatic crystals kept in cold storage. Nature 506, 480–483. https://doi.org/10.1038/Nature12991.

Cooper, G.F., Wilson, C.J.N., 2014. Development, mobilisation and eruption of a large crystal-rich rhyolite: the Ongatiti ignimbrite, New Zealand. Lithos 198–199, 38–57. https://doi.org/10.1016/j.lithos.2014.03.014.

Cordonnier, B., Hess, K.-U., Lavallee, Y., Dingwell, D.B., 2009. Rheological properties of dome lavas: case study of Unzen volcano. Earth Planet. Sci. Lett. 279, 263–272. https://doi.org/10.1016/j.epsl.2009.01.014.

Cordonnier, B., Caricchi, L., Pistone, M., Castro, J., Hess, K.-U., Gottschaller, S., Manga, M., Dingwell, D., Burlini, L., 2012. The viscous-brittle transition of crystal-bearing silicic melt: direct observation of magma rupture and healing. Geology 40, 611–614.

Costa, A., Smith, V.C., Macedonio, G., Matthews, N.E., 2014. The magnitude and impact of the Youngest Toba Tuff super-eruption. Front. Earth Sci. 2 https://doi.org/10.3389/feart.2014.00016.

Crisp, L.J., Berry, A.J., 2022. A new model for zircon saturation in silicate melts. Contrib. Mineral. Petrol. 177, 71. https://doi.org/10.1007/s00410-022-01925-6.

Danišík, M., Schmitt, A.K., Stockli, D.F., Lovera, O.M., Dunkl, I, Evans, N.J., 2017. Application of combined U-Th-disequilibrium/U-Pb and (U-Th)/He zircon dating to tephrochronology. Quat. Geochronol. 40, 23–32. https://doi.org/10.1016/j.quageo.2016.07.005.

Dash, S.K., 2005. Monsoons and monsoon climate. In: Oliver, J.E. (Ed.), Encyclopedia of World Climatology. Springer Netherlands, Dordrecht, pp. 509–516. https://doi.org/10.1007/1-4020-3266-8_142.

Daud, Y., 2001. Sibayak geothermal field (Indonesia): structure assessed from gravity and hydrogeological considerations. Geotherm. Resour. Council Trans. 25, 395–399.

de Silva, S.L., Mucek, A.E., Gregg, P.M., Pratomo, I., 2015. Resurgent Toba—Field, chronologic, and model constraints on time scales and mechanisms of resurgence at large calderas. Front. Earth Sci. 3, 25.

Deering, C.D., Bachmann, O., 2010. Trace element indicators of crystal accumulation in silicic igneous rocks. Earth Planet. Sci. Lett. 297, 324–331. https://doi.org/10.1016/J.Epsl.2010.06.034.

Di Salvo, S., Avanzinelli, R., Isaia, R., Zanetti, A., Druitt, T., Francalanci, L., 2020. Crystal-mush reactivation by magma recharge: evidence from the Campanian Ignimbrite activity, Campi Flegrei volcanic field, Italy. Lithos 376–377, 105780. https://doi.org/10.1016/j.lithos.2020.105780.

Druitt, T.H., Edwards, L., Mellors, R., Pyle, D., Sparks, R., Lanphere, M., Davies, M., Barreirio, B., 1999. Santorini volcano. Geol. Soc. Mem. 19.

Edmonds, M., Cashman, K.V., Holness, M., Jackson, M., 2019. Architecture and dynamics of magma reservoirs. Philos. Trans. R. Soc. A Math. Phys. Eng. Sci. 377, 20180298. https://doi.org/10.1098/rsta.2018.0298.

Ellis, B.S., Neukampf, J., Bachmann, O., Harris, C., Forni, F., Magna, T., Laurent, O., Ulmer, P., 2022. Biotite as a recorder of an exsolved Li-rich volatile phase in upper-crustal silicic magma reservoirs. Geology 50, 481–485. https://doi.org/10.1130/G49484.1.

Ellis, B.S., Wolff, J.A., Szymanowski, D., Forni, F., Cortes-Calderon, E.A., Bachmann, O., 2023. Cumulate recycling in igneous systems: the volcanic record. Lithos 456–457, 107284. https://doi.org/10.1016/j.lithos.2023.107284.

Fabbro, G.N., Druitt, T.H., Costa, F., 2017. Storage and eruption of silicic magma across the transition from dominantly effusive to caldera-forming states at an arc volcano (Santorini, Greece). J. Petrol. 58, 2429–2464. https://doi.org/10.1093/petrology/egy013.

Fauzi, McCaffrey, R., Wark, D., Sunaryo, Prih Haryadi, P.Y., 1996. Lateral variation in slab orientation beneath Toba Caldera, northern Sumatra. Geophys. Res. Lett. 23, 443–446. https://doi.org/10.1029/96GL00381.

Fedele, L., Scarpati, C., Lanphere, M., Melluso, L., Morra, V., Perrotta, A., Ricci, G., 2008. The Breccia Museo formation, Campi Flegrei, Southern Italy: geochronology, chemostratigraphy and relationship with the Campanian Ignimbrite eruption. Bull. Volcanol. 70, 1189–1219. https://doi.org/10.1007/S00445-008-0197-Y.

Ferry, J.M., Watson, E.B., 2007. New thermodynamic models and revised calibrations for the Ti-in-zircon and Zr-in-rutile thermometers. Contrib. Mineral. Petrol. 154, 429–437. https://doi.org/10.1007/s00410-007-0201-0.

Flowers, R.M., Ketcham, R.A., Enkelmann, E., Gautheron, C., Reiners, P.W., Metcalf, J.R., Danišík, M., Stockli, D.F., Brown, R.W., 2022. (U-Th)/He chronology: part 2. Considerations for evaluating, integrating, and interpreting conventional individual aliquot data. GSA Bull. 135, 137–161. https://doi.org/10.1130/B36268.1.

Foley, M.L., Miller, C.F., Gualda, G.A.R., 2020. Architecture of a super-sized magma chamber and remobilization of its basal cumulate (Peach Spring Tuff, USA). J. Petrol. https://doi.org/10.1093/petrology/egaa020.

Forni, F., Bachmann, O., Mollo, S., De Astis, G., Gelman, S.E., Ellis, B.S., 2016. The origin of a zoned ignimbrite: insights into the Campanian Ignimbrite magma chamber (Campi Flegrei, Italy). Earth Planet. Sci. Lett. 449, 259–271. https://doi.org/10.1016/j.epsl.2016.06.003.

Gebauer, S.K., Schmitt, A.K., Pappalardo, L., Stockli, D.F., Lovera, O.M., 2014. Crystallization and eruption ages of Breccia Museo (Campi Flegrei caldera, Italy) plutonic clasts and their relation to the Campanian ignimbrite. Contrib. Mineral. Petrol. 167, 1–18. Artn 953. https://doi.org/10.1007/S00410-013-0953-7.

Ghiorso, M.S., Evans, B.W., 2008. Thermodynamics of rhombohedral oxide solid solutions and a revision of the FE-TI two-oxide geothermometer and oxygen-barometer. Am. J. Sci. 308, 957–1039. https://doi.org/10.2475/09.2008.01.

Giordano, D., Russell, J.K., Dingwell, D.B., 2008. Viscosity of magmatic liquids: a model. Earth Planet. Sci. Lett. 271, 123–134. https://doi.org/10.1016/j.epsl.2008.03.038.

Girard, G., Stix, J., 2012. Future Volcanism at Yellowstone Caldera: Insights from Geochemistry of Young Volcanic Units and Monitoring of Volcanic Unrest.

Gleadow, A., Harrison, M., Kohn, B., Lugo-Zazueta, R., Phillips, D., 2015. The Fish Canyon Tuff: a new look at an old low-temperature thermochronology standard. Earth Planet. Sci. Lett. 424, 95–108. https://doi.org/10.1016/j.epsl.2015.05.003.

Gonnermann, H.M., Manga, M., 2013. Dynamics of magma ascent in the Modeling volcanic processes: The physics and mathematics of volcanism, 55.

Grootes, P.M., Hughen, K.A., Kromer, B., Reimer, P.J., Adkins, J., Burke, A., Cook, M.S., Olsen, J., Skinner, L.C., 2020. Marine20—The Marine Radiocarbon Age Calibration Curve (0–55,000 cal BP). Radiocarbon 62, 779–820. https://doi.org/10.1017/RDC.2020.68.

Gualda, G.A.R., Ghiorso, M.S., Lemons, R.V., Carley, T.L., 2012. Rhyolite-MELTS: a modified calibration of MELTS optimized for silica-rich, fluid-bearing magmatic systems. J. Petrol. 53, 875–890. https://doi.org/10.1093/petrology/egr080.

Guillong, M., Sliwinski, J.T., Schmitt, A., Forni, F., Bachmann, O., 2016. U-Th zircon dating by laser ablation single collector inductively coupled plasma-mass

spectrometry (LA-ICP-MS). Geostand Geoanal Res. https://doi.org/10.1111/j.1751-908X.2016.00396.x.

Hamilton, W.B., 1979. Tectonics of the Indonesian Region. US Government Printing Office.

Hebbeln, D., 2006. Report and Preliminary Results of RV Sonne Cruise SO-184, Pabesia, Durban (South Africa)-Cilacap (Indonesia)-Darwin (Australia), July 8th-September 13th, 2005. Berichte aus dem Fachbereich Geowissenschaften der Universität Bremen.

Hildreth, W., 1981. Gradients in silicic magma chambers - implications for lithospheric magmatism. J. Geophys. Res. 86, 153–192. https://doi.org/10.1029/Jb086ib11p10153.

Hildreth, W., Wilson, C.J.N., 2007. Compositional zoning of the Bishop Tuff. J. Petrol. 48, 951–999. https://doi.org/10.1093/Petrology/Egm007.

Holland, T., Blundy, J., 1994. Non-ideal interactions in calcic amphiboles and their bearing on amphibole-plagioclase thermometry. Contrib. Mineral. Petrol. 116, 433–447. https://doi.org/10.1007/BF00310910.

Hou, T., Botcharnikov, R., Moulas, E., Just, T., Berndt, J., Koepke, J., Zhang, Z., Wang, M., Yang, Z., Holtz, F., 2020. Kinetics of Fe-Ti oxide re-equilibration in magmatic systems: implications for thermo-oxybarometry. J. Petrol. 61 (11−12) p. egaa116.

Hourigan, J.K., Reiners, P.W., Brandon, M.T., 2005. U-Th zonation-dependent alpha-ejection in (U-Th)/He chronometry. Geochim. Cosmochim. Acta 69, 3349–3365. https://doi.org/10.1016/j.gca.2005.01.024.

Huber, C., Bachmann, O., Dufek, J., 2011. Thermo-mechanical reactivation of locked crystal mushes: melting-induced internal fracturing and assimilation processes in magmas. Earth Planet. Sci. Lett. 304, 443–454. https://doi.org/10.1016/J.Epsl.2011.02.022.

Huber, C., Bachmann, O., Dufek, J., 2012. Crystal-poor versus crystal-rich ignimbrites: a competition between stirring and reactivation. Geology 40, 115–118. https://doi.org/10.1130/G32425.1.

Huber, C., Townsend, M., Degruyter, W., Bachmann, O., 2019. Optimal depth of subvolcanic magma chamber growth controlled by volatiles and crust rheology. Nat. Geosci. 12, 762–768. https://doi.org/10.1038/s41561-019-0415-6.

Karakas, O., Degruyter, W., Bachmann, O., Dufek, J., 2017. Lifetime and size of shallow magma bodies controlled by crustal-scale magmatism. Nat. Geosci. 10, 446–450. https://doi.org/10.1038/ngeo2959. http://www.nature.com/ngeo/journal/v10/n6/abs/ngeo2959.html#supplementary-information.

Karlstrom, L., Dufek, J., Manga, M., 2009. Organization of volcanic plumbing through magmatic lensing by magma chambers and volcanic loads. J. Geophys. Res. Solid Earth 114. https://doi.org/10.1029/2009JB006339.

Karstens, J., Preine, J., Crutchley, G.J., Kutterolf, S., van der Bilt, W.G.M., Hooft, E.E.E., Druitt, T.H., Schmid, F., Cederstrøm, J.M., Hübscher, C., Nomikou, P., Carey, S., Kühn, M., Elger, J., Berndt, C., 2023. Revised Minoan eruption volume as benchmark for large volcanic eruptions. Nat. Commun. 14, 2497. https://doi.org/10.1038/s41467-023-38176-3.

Keller, C.B., Schoene, B., Samperton, K.M., 2018. A stochastic sampling approach to zircon eruption age interpretation. Geochem. Persp. Lett. 8, 31–35. https://doi.org/10.7185/geochemlet.1826.

Keller, F., Bachmann, O., Geshi, N., Miyakawa, A., 2021. The role of crystal accumulation and cumulate remobilization in the formation of large zoned ignimbrites: insights from the Aso-4 caldera-forming eruption, Kyushu, Japan. Front. Earth Sci. 8 https://doi.org/10.3389/feart.2020.614267.

Kennedy, B., Wilcock, J., Stix, J., 2012. Caldera resurgence during magma replenishment and rejuvenation at Valles and Lake City calderas. Bull. Volcanol. 74, 1833–1847.

Ketcham, R.A., Gautheron, C., Tassan-Got, L., 2011. Accounting for long alpha-particle stopping distances in (U–Th–Sm)/He geochronology: refinement of the baseline case. Geochim. Cosmochim. Acta 75, 7779–7791. https://doi.org/10.1016/j.gca.2011.10.011.

Klemetti, E.W., Clynne, M.A., 2014. Localized rejuvenation of a crystal mush recorded in zircon temporal and compositional variation at the Lassen Volcanic Center, Northern California. PLoS ONE 9, e113157. https://doi.org/10.1371/journal.pone.0113157.

Kolzenburg, S., Chevrel, M.O., Dingwell, D.B., 2022. Magma/suspension rheology. Rev. Mineral. Geochem. 87, 639–720. https://doi.org/10.2138/rmg.2022.87.14.

Koulakov, I., Kasatkina, E., Shapiro, N.M., Jaupart, C., Vasilevsky, A., El Khrepy, S., Al-Arifi, N., Smirnov, S., 2016. The feeder system of the Toba supervolcano from the slab to the shallow reservoir. Nat. Commun. 7, 12228. https://doi.org/10.1038/ncomms12228.

Kushnir, A.R.L., Martel, C., Champallier, R., Wadsworth, F.B., 2017. Permeability evolution in variably glassy basaltic andesites measured under magmatic conditions. Geophys. Res. Lett. 44, 10262–10271. https://doi.org/10.1002/2017GL074042.

Kutterolf, S., Schindlbeck-Belo, J.C., Müller, F., Pank, K., Lee, H.Y., Wang, K.L., Schmitt, A.K., 2023. Revisiting the occurrence and distribution of Indian Ocean Tephra: quaternary marine Toba ash inventory. J. Volcanol. Geotherm. Res. 441, 107879.

Le Bas, M.J., Le Maitre, R.W., Streckeisen, A., Zanettin, B., IUGS Subcommission on the Systematics of Igneous Rocks, 1986. A chemical classification of volcanic rocks based on the total alkali-silica diagram. J. Petrol. 27, 745–750. https://doi.org/10.1093/petrology/27.3.745.

Legros, F., 2000. Minimum volume of a tephra fallout deposit estimated from a single isopach. J. Volcanol. Geotherm. Res. 96, 25–32. https://doi.org/10.1016/S0377-0273(99)00135-3.

Lindoo, A., Larsen, J., Cashman, K., Oppenheimer, J., 2017. Crystal controls on permeability development and degassing in basaltic andesite magma. Geology 45, 831–834.

Liu, Y., Zhang, Y., Behrens, H., 2005. Solubility of H_2O in rhyolitic melts at low pressures and a new empirical model for mixed $H_2O–CO_2$ solubility in rhyolitic melts.

J. Volcanol. Geotherm. Res. 143, 219–235. https://doi.org/10.1016/j.jvolgeores.2004.09.019.

Lo, J.C.-F., Orton, T., 2016. The general features of tropical Sumatra Squalls. Weather 71, 175–178. https://doi.org/10.1002/wea.2748.

Lougheed, B.C., Obrochta, S.P., 2016. MatCal: open source Bayesian 14C age calibration in Matlab. J. Open Res. Softw. https://doi.org/10.5334/jors.130.

Mark, D.F., Petraglia, M., Smith, V.C., Morgan, L.E., Barfod, D.N., Ellis, B.S., Pearce, N.J., Pal, J.N., Korisettar, R., 2014. A high-precision 40Ar/39Ar age for the Young Toba Tuff and dating of ultra-distal tephra: forcing of Quaternary climate and implications for hominin occupation of India. Quat. Geochronol. 21, 90–103. https://doi.org/10.1016/j.quageo.2012.12.004.

Mark, D.F., Renne, P.R., Dymock, R.C., Smith, V.C., Simon, J.I., Morgan, L.E., Staff, R.A., Ellis, B.S., Pearce, N.J.G., 2017. High-precision 40Ar/39Ar dating of pleistocene tuffs and temporal anchoring of the Matuyama-Brunhes boundary. Quat. Geochronol. 39, 1–23. https://doi.org/10.1016/j.quageo.2017.01.002.

Marxer, F., Ulmer, P., 2019. Crystallisation and zircon saturation of calc-alkaline tonalite from the Adamello Batholith at upper crustal conditions: an experimental study. Contrib. Mineral. Petrol. 174, 84. https://doi.org/10.1007/s00410-019-1619-x.

Matthews, N.E., Pyle, D.M., Smith, V.C., Wilson, C.J.N., Huber, C., van Hinsberg, V., 2012. Quartz zoning and the pre-eruptive evolution of the ~340-ka Whakamaru magma systems, New Zealand. Contrib. Mineral. Petrol. 163, 87–107. https://doi.org/10.1007/s00410-011-0660-1.

McCaffrey, R., 1991. Slip vectors and stretching of the Sumatran fore arc. Geology 19, 881–884.

McCaffrey, R., Zwick, P.C., Bock, Y., Prawirodirdjo, L., Genrich, J.F., Stevens, C.W., Puntodewo, S.S.O., Subarya, C., 2000. Strain partitioning during oblique plate convergence in northern Sumatra: geodetic and seismologic constraints and numerical modeling. J. Geophys. Res. Solid Earth 105, 28363–28376. https://doi.org/10.1029/1999JB900362.

McDonough, W.F., Sun, S.S., 1995. The composition of the Earth. Chem. Geol. 120, 223–253. https://doi.org/10.1016/0009-2541(94)00140-4.

Molloy, C., Shane, P., Nairn, I., 2008. Pre-eruption thermal rejuvenation and stirring of a partly crystalline rhyolite pluton revealed by the Earthquake Flat Pyroclastics deposits, New Zealand. J. Geol. Soc. London 165, 435–447. https://doi.org/10.1144/0016-76492007-071.

Mucek, A.E., Danišík, M., de Silva, S.L., Schmitt, A.K., Pratomo, I., Coble, M.A., 2017. Post-supereruption recovery at Toba Caldera. Nat. Commun. 8, 15248. https://doi.org/10.1038/ncomms15248.

Ninkovich, D., Sparks, R.S.J., Ledbetter, M.T., 1978. The exceptional magnitude and intensity of the Toba eruption, Sumatra: an example of the use of deep-sea tephra layers as a geological tool. Bull. Volcanol. 41, 286. https://doi.org/10.1007/BF02597228.

Pallister, J.S., Hoblitt, R.P., Reyes, A.G., 1992. A basalt trigger for the 1991 eruptions of Pinatubo volcano? Nature 356, 426–428.

Pansino, S., Taisne, B., 2019. How magmatic storage regions attract and repel propagating dikes. J. Geophys. Res. Solid Earth 124, 274–290. https://doi.org/10.1029/2018JB016311.

Paton, C., Woodhead, J.D., Hellstrom, J.C., Hergt, J.M., Greig, A., Maas, R., 2010. Improved laser ablation U-Pb zircon geochronology through robust downhole fractionation correction. Geochem. Geophys. Geosyst. 11.

Paton, C., Hellstrom, J., Paul, B., Woodhead, J., Hergt, J., 2011. Iolite: Freeware for the visualisation and processing of mass spectrometric data. J. Anal. At. Spectrom 26, 2508–2518.

Pearce, N.J.G., Perkins, W.T., Westgate, J.A., Wade, S.C., 2011. Trace-element microanalysis by LA-ICP-MS: the quest for comprehensive chemical characterisation of single, sub-10 μm volcanic glass shards. Quat. Int. 246, 57–81. https://doi.org/10.1016/j.quaint.2011.07.012.

Phua, M., 2022. A Quaternary Record of Explosive Eruptions along the Western Sunda Volcanic Arc: Insights into the Eruptive Histories of Volcanoes in Sumatra, Indonesia (Doctoral Thesis). Nanyang Technological University, Singapore.

Pollard, T., Woodhead, J., Hellstrom, J., Engel, J., Powell, R., Drysdale, R., 2023. \texttt{DQPB}: software for calculating disequilibrium U–Pb ages. Geochronology 5, 181–196. https://doi.org/10.5194/gchron-5-181-2023.

Popa, R.-G., Bachmann, O., Huber, C., 2021. Explosive or effusive style of volcanic eruption determined by magma storage conditions. Nat. Geosci. 14, 781–786. https://doi.org/10.1038/s41561-021-00827-9.

Prawirodirdjo, L., Bock, Y., Genrich, J.F., Puntodewo, S.S.O., Rais, J., Subarya, C., Sutisna, dam S., 2000. One century of tectonic deformation along the Sumatran fault from triangulation and Global Positioning System surveys. J. Geophys. Res. Solid Earth 105, 28343–28361.

Putirka, K., 2008. Thermometers and barometers for volcanic systems. Rev. Miner. Geochem. 69, 61–120.

Putirka, K., 2016. Amphibole thermometers and barometers for igneous systems and some implications for eruption mechanisms of felsic magmas at arc volcanoes. Am. Mineral. 101, 841–858.

Reid, M.R., Coath, C.D., Harrison, T.M., McKeegan, K.D., 1997. Prolonged residence times for the youngest rhyolites associated with Long Valley Caldera: Th-230-U-238 ion microprobe dating of young zircons. Earth Planet. Sci. Lett. 150, 27–39. https://doi.org/10.1016/S0012-821x(97)00077-0.

Reid, M.R., Vazquez, J.A., Schmitt, A.K., 2011. Zircon-scale insights into the history of a Supervolcano, Bishop Tuff, Long Valley, California, with implications for the Ti-in-zircon geothermometer. Contrib. Mineral. Petrol. 161, 293–311.

Reimer, P.J., Austin, W.E.N., Bard, E., Bayliss, A., Blackwell, P.G., Bronk Ramsey, C., Butzin, M., Cheng, H., Edwards, R.L., Friedrich, M., Grootes, P.M., Guilderson, T.P., Hajdas, I., Heaton, T.J., Hogg, A.G., Hughen, K.A., Kromer, B., Manning, S.W., Muscheler, R., Palmer, J.G., Pearson, C., van der Plicht, J., Reimer, R.W.,

Richards, D.A., Scott, E.M., Southon, J.R., Turney, C.S.M., Wacker, L., Adolphi, F., Büntgen, U., Capano, M., Fahrni, S.M., Fogtmann-Schulz, A., Friedrich, R., Köhler, P., Kudsk, S., Miyake, F., Olsen, J., Reinig, F., Sakamoto, M., Sookdeo, A., Talamo, S., 2020. The IntCal20 northern hemisphere radiocarbon age calibration curve (0–55 cal kBP). Radiocarbon 62, 725–757. https://doi.org/10.1017/RDC.2020.41.

Repstock, A., Breitkreuz, C., Lapp, M., Schulz, B., 2018. Voluminous and crystal-rich igneous rocks of the Permian Wurzen volcanic system, northern Saxony, Germany: physical volcanology and geochemical characterization. Int. J. Earth Sci. 107, 1485–1513. https://doi.org/10.1007/s00531-017-1554-x.

Ridolfi, F., Renzulli, A., 2012. Calcic amphiboles in calc-alkaline and alkaline magmas: thermobarometric and chemometric empirical equations valid up to 1,130°C and 2.2 GPa. Contrib. Mineral. Petrol. 163, 877–895. https://doi.org/10.1007/s00410-011-0704-6.

Roduit, N., 2007. JMicroVision: un logiciel d'analyse d'images pétrographiques polyvalent. Section des Sciences de la Terre, Université de Genève.

Rose, W.I., Chesner, C.A., 1987. Dispersal of ash in the great Toba eruption, 75 ka. Geology 15, 913–917. https://doi.org/10.1130/0091-7613(1987)15<913:Doaitg>2.0.Co;2.

Rowe, M.C., Ellis, B.S., Lindeberg, A., 2012. Quantifying crystallization and devitrification of rhyolites by means of X-ray diffraction and electron microprobe analysis. Am. Mineral. 97, 1685–1699. https://doi.org/10.2138/am.2012.4006.

Rutherford, M.J., Hill, P.M., 1993. Magma ascent rates from amphibole breakdown: an experimental study applied to the 1980–1986 Mount St. Helens eruptions. J. Geophys. Res. Solid Earth 98, 19667–19685. https://doi.org/10.1029/93JB01613.

Salisbury, M.J., Patton, J.R., Kent, A.J.R., Goldfinger, C., Djadjadihardja, Y., Hanifa, U., 2012. Deep-sea ash layers reveal evidence for large, late Pleistocene and Holocene explosive activity from Sumatra, Indonesia. J. Volcanol. Geotherm. Res. 231–232, 61–71. https://doi.org/10.1016/j.jvolgeores.2012.03.007.

Schmitt, A.K., Stockli, D.F., Niedermann, S., Lovera, O.M., Hausback, B.P., 2010. Eruption ages of Las Tres Vírgenes volcano (Baja California): a tale of two helium isotopes. Quat. Geochronol. 5, 503–511. https://doi.org/10.1016/j.quageo.2010.02.004.

Singer, B.S., Andersen, N.L., Le Mével, H., Feigl, K.L., DeMets, C., Tikoff, B., Thurber, C.H., Jicha, B.R., Cardona, C., Córdova, L., 2014. Dynamics of a large, restless, rhyolitic magma system at Laguna del Maule, southern Andes, Chile. GSA Today 24, 4–10.

Sliwinski, J.T., Bachmann, O., Dungan, M.A., Huber, C., Deering, C.D., Lipman, P.W., Martin, L.H.J., Liebske, C., 2017. Rapid pre-eruptive thermal rejuvenation in a large silicic magma body: the case of the Masonic Park Tuff, Southern Rocky Mountain volcanic field, CO, USA. Contrib. Mineral. Petrol. 172, 30. https://doi.org/10.1007/s00410-017-1351-3.

Sparks, S.R., Sigurdsson, H., Wilson, L., 1977. Magma mixing: a mechanism for triggering acid explosive eruptions. Nature 267, 315–318.

Southon, J., Kashgarian, M., Fontugne, M., Metivier, B.W.-S., Yim, W., 2002. Marine Reservoir Corrections for the Indian Ocean and Southeast Asia. Radiocarbon 44, 167–180. https://doi.org/10.1017/S0033822200064778.

Szymanowski, D., Wotzlaw, J.-F., Ellis, B.S., Bachmann, O., Guillong, M., von Quadt, A., 2017. Protracted near-solidus storage and pre-eruptive rejuvenation of large magma reservoirs. Nat. Geosci. 10, 777–782. https://doi.org/10.1038/ngeo3020.

Szymanowski, D., Fehr, M.A., Guillong, M., Coble, M.A., Wotzlaw, J.-F., Nasdala, L., Ellis, B.S., Bachmann, O., Schönbächler, M., 2018. Isotope-dilution anchoring of zircon reference materials for accurate Ti-in-zircon thermometry. Chem. Geol. 481, 146–154. https://doi.org/10.1016/j.chemgeo.2018.02.001.

Szymanowski, D., Ellis, B.S., Wotzlaw, J.-F., Bachmann, O., 2019. Maturation and rejuvenation of a silicic magma reservoir: high-resolution chronology of the Kneeling Nun Tuff. Earth Planet. Sci. Lett. 510, 103–115. https://doi.org/10.1016/j.epsl.2019.01.007.

Szymanowski, D., Forni, F., Phua, M., Jicha, B., Lee, D.W.J., Hsu, Y.-J., Rifai, H., Schoene, B., Bouvet de Maisonneuve, C., 2023. A shifty Toba magma reservoir: Improved eruption chronology and petrochronological evidence for lateral growth of a giant magma body. Earth and Planetary Science Letters 622, 118408. https://doi.org/10.1016/j.epsl.2023.118408.

Szymanowski, D., Forni, F., Wolff, J.A., Ellis, B.S., 2020. Modulation of zircon solubility by crystal–melt dynamics. Geology 48, 798–802.

Tapster, S., Condon, D.J., Naden, J., Noble, S.R., Petterson, M.G., Roberts, N.M.W., Saunders, A.D., Smith, D.J., 2016. Rapid thermal rejuvenation of high-crystallinity magma linked to porphyry copper deposit formation; evidence from the Koloula Porphyry Prospect, Solomon Islands. Earth Planet. Sci. Lett. 442, 206–217. https://doi.org/10.1016/j.epsl.2016.02.046.

Tavazzani, L., Peres, S., Sinigoi, S., Demarchi, G., Economos, R., Quick, J., 2020. Timescales and mechanisms of crystal-mush rejuvenation and melt extraction recorded in Permian plutonic and volcanic rocks of the Sesia Magmatic System (southern Alps, Italy). J. Petrol. 61, egaa049.

Tierney, C.R., Schmitt, A.K., Lovera, O.M., de Silva, S.L., 2016. Voluminous plutonism during volcanic quiescence revealed by thermochemical modeling of zircon. Geology 44, 683–686. https://doi.org/10.1130/G37968.1.

Till, C.B., Vazquez, J.A., Stelten, M.E., Shamloo, H.I., Shaffer, J.S., 2019. Coexisting discrete bodies of rhyolite and punctuated volcanism characterize Yellowstone's post-Lava Creek Tuff caldera evolution. Geochem. Geophys. Geosyst. 20, 3861–3881.

Townsend, M., Huber, C., Degruyter, W., Bachmann, O., 2019. Magma chamber growth during intercaldera periods: insights from thermo-mechanical modeling with applications to Laguna del Maule, Campi Flegrei, Santorini, and Aso. Geochem. Geophys. Geosyst. 20, 1574–1591. https://doi.org/10.1029/2018GC008103.

Van Padang, M.N., 1983. History of the Volcanology in the Former Netherlands East Indies. Citeseer.

Vermeesch, P., 2018. IsoplotR: a free and open toolbox for geochronology. Geosci. Front. 9, 1479–1493. https://doi.org/10.1016/j.gsf.2018.04.001.

Ward, K.M., Zandt, G., Beck, S.L., Christensen, D.H., McFarlin, H., 2014. Seismic imaging of the magmatic underpinnings beneath the Altiplano-Puna volcanic complex from the joint inversion of surface wave dispersion and receiver functions. Earth Planet. Sci. Lett. 404, 43–53. https://doi.org/10.1016/j.epsl.2014.07.022.

Wark, D.A., Hildreth, W., Spear, F.S., Cherniak, D.J., Watson, E.B., 2007. Pre-eruption recharge of the Bishop magma system. Geology 35, 235–238. https://doi.org/10.1130/G23316a.1.

Waters, L.E., Lange, R.A., 2015. An updated calibration of the plagioclase-liquid hygrometer-thermometer applicable to basalts through rhyolites. Am. Mineral. 100, 2172–2184. https://doi.org/10.2138/am-2015-5232.

Watts, L.E., John, D.A., Colgan, J.P., Henry, C.D., Bindeman, I.N., Schmitt, A.K., 2016. Probing the Volcanic–Plutonic Connection and the Genesis of Crystal-rich Rhyolite in a Deeply Dissected Supervolcano in the Nevada Great Basin: Source of the Late Eocene Caetano Tuff. J. Petrol. 57, 1599–1644. https://doi.org/10.1093/petrology/egw051.

Westerveld, J., 1952. Quaternary Volcanism on Sumatra. GSA Bull. 63, 561–594. https://doi.org/10.1130/0016-7606(1952)63[561:Qvos]2.0.Co;2.

Whelley, P.L., Newhall, C.G., Bradley, K.E., 2015. The frequency of explosive volcanic eruptions in Southeast Asia. Bull. Volcanol. 77, 1. https://doi.org/10.1007/s00445-014-0893-8.

Wolff, J.A., Gardner, J.N., 1995. Is the Valles Caldera entering a new cycle of activity. Geology 23, 411–414. https://doi.org/10.1130/0091-7613(1995)023<0411:Itvcea>2.3.Co;2.

Wolff, J.A., Neukampf, J., 2022. Biotite as an indicator of post-eruptive cryptic alteration in the Battleship Rock Ignimbrite, Valles Caldera, NM, USA. Bull. Volcanol. 84, 99. https://doi.org/10.1007/s00445-022-01609-w.

Wolff, J.A., Storey, M., 1984. Zoning in highly alkaline magma bodies. Geol. Mag. 121, 563–575.

Wolff, J.A., Ellis, B.S., Ramos, F.C., Starkel, W.A., Boroughs, S., Olin, P.H., Bachmann, O., 2015. Remelting of cumulates as a process for producing chemical zoning in silicic tuffs: a comparison of cool, wet and hot, dry rhyolitic magma systems. Lithos 236–237, 275–286. https://doi.org/10.1016/j.lithos.2015.09.002.

Wolff, J.A., Forni, F., Ellis, B.S., Szymanowski, D., 2020. Europium and barium enrichments in compositionally zoned felsic tuffs: a smoking gun for the origin of chemical and physical gradients by cumulate melting. Earth Planet. Sci. Lett. 540, 116251.

Wotzlaw, J.-F., Schaltegger, U., Frick, D.A., Dungan, M.A., Gerdes, A., Günther, D., 2013. Tracking the evolution of large-volume silicic magma reservoirs from assembly to supereruption. Geology 41, 867–870. https://doi.org/10.1130/G34366.1.

Zhao, S., Xia, Y., Xu, X., Zhao, K., 2023. Timescale of magma recharge for a crystal-rich mush: perspectives from the compositional zoned quartz in Xiangshan caldera, SE China. Lithos 456, 107288.